Westfälische Wilhelms-Universität Münster
Institut für Kernphysik
AG Andronic

Bachelor's Thesis in Physics

χ_c meson reconstruction from pp collisions at the LHC

Jannik Tim Zarnitz (E-Mail: jannik.zarnitz@uni-muenster.de)

First examiner: Prof. Dr. Anton Andronic
Second examiner: Apl. Prof. Dr. Christian Klein-Bösing

September 29, 2022

Contents

1 Introduction **1**

2 Theoretical principles **2**

2.1 The Standard Model of particle physics 2

2.2 V^0 particles and decays 5

2.2.1 Overview about V^0 decays 5

2.2.2 Weak interaction 8

2.2.3 Pair production and photon conversion 9

2.3 Charmonium 11

3 The ALICE Detector **16**

3.1 The ALICE Experiment at the LHC 16

3.1.1 The LHC at CERN 16

3.1.2 ALICE Detector Layout 18

3.1.3 The Inner Tracking System 20

3.1.4 The V0 Detector 21

3.1.5 The Time Projection Chamber 22

3.2 Particle Identification 23

3.2.1 Tracking 23

3.2.2 V^0 Detection 28

4 Data analysis **32**

5 Conclusions **43**

References **45**

1 Introduction

In this thesis the reconstruction of χ_c mesons from proton–proton collisions at a centre-of-mass energy of $\sqrt{s} = 13\,\text{TeV}$ at the Large Hadron Collider is performed. The χ_c meson is identified through its $\gamma J/\psi$ decay channel using Run-2 ESD data collected by the ALICE detector in 2016. In total, there are over 630 million minimum bias triggered events provided.

Strictly speaking, the χ_c with $L = 1$ (1P) is a spin triplet state including the χ_{c0}, the χ_{c1} and the χ_{c2}. While reconstructing the J/ψ from the e^+e^- decay channel, the photons are gathered by using the V^0 topology. Tracking and particle identification is accomplished by mainly using three subdetectors of the ALICE detector: the ITS, the V0 and the TPC. In doing so, there are multiple sorts of cuts applied, which include the standard track cuts for the J/ψ analysis and loose cuts for the detection of photons.

The J/ψ are reconstructed successfully. By reducing the background, the J/ψ signal becomes readily visible and is extracted. The number of obtained J/ψ is in agreement with the rough estimation of 2 J/ψ per million events, which are expected for minimum biased data and standard track cuts.

Throughout the whole analysis process, a distinction is made between offline photons and on the fly photons, as they are classified as V^0 particles. The photons turn out to be suitable for the χ_c analysis. Particularly because their momentum reaches down to low values.

In the resulting invariant mass distributions of the reconstructed χ_c candidates, there are no peaks visible that can be associated to one of the three χ_{cJ} states. This means that the χ_c signal vanishes in the background. To conclude, the χ_c reconstruction is limited in statistics because the number of available events in the analysis is not high enough. Thus, more data is required. However, it can be roughly estimated how many events are needed to detect one χ_c. Ultimately, one has to process an approximate number of 24 million events to obtain one χ_c. There are also other signal enhancement methods that could be applied in further studies.

2 Theoretical principles

Before diving into the reconstruction of χ_c mesons, some basic theory needs to be discussed.

2.1 The Standard Model of particle physics

The Standard Model of particle physics is a theory that describes how three of the four known fundamental forces of nature and all known fundamental particles are related to each other [1]. These also called elementary particles are divided into four categories: quarks, leptons, gauge and scalar bosons. In total, there are six quarks and six leptons as well as their corresponding antiparticles. Every particle X is associated with an antiparticle $\overline{X}$ that possesses X's mass and spin but the opposite charge. Particles with a half-integer spin are called fermions, which includes quarks, leptons and all forms of so-called baryons. A baryon is a bound state of three quarks and an anti-baryon, on the other hand, is composed of three antiquarks. Protons (uud) and neutrons (udd) are the most prominent examples of baryons. Speaking of bound quark states, quarks and antiquarks can also pair up to form particles that are called mesons. These mesons are either quark-quark, quark-antiquark or antiquark-antiquark pairs. Their spin is always an integer, which means that they are classified as bosons. Some of the most familiar examples of mesons are the charged pions π^+ ($u\overline{d}$) and π^- ($d\overline{u}$). Even the famous J/ψ ($c\overline{c}$) and its excited states like the χ_c count among the mesons. Generally speaking, when a particle consists of quarks or antiquarks, it is referred to as a hadron. Table 1 gives an overview of the fermions that are defined in the Standard Model of particle physics.

Table 1: The three different generations of quarks and leptons as defined in the Standard Model of particle physics. The fermions are organised in three generations representing some kind of mass hierarchy [2].

Fermion	1st generation	2nd generation	3rd generation	Charge
Quarks	Up (u)	Charm (c)	Top (t)	$+\frac{2}{3}$
	Down (d)	Strange (s)	Bottom (b)	$-\frac{1}{3}$
Leptons	Electron (e^-)	Muon (μ^-)	Tauon (τ^-)	-1
	Electron neutrino (ν_e)	Muon neutrino (ν_μ)	Tauon neutrino (ν_τ)	0

Quarks and antiquarks are said to be colour charged particles, which means that every quark or antiquark carries a colour charge. Following the additive colour model, one differentiates between six colour charges: red, blue and green for particles as well as antired, antiblue and antigreen for antiparticles. Mixing all three different colours or pairing one colour with its complement anticolour results in a net colour charge of zero. Naturally, the same happens for putting together all the three different anticolours. Once a particle has a colour charge of zero, one refers to it as neutral colour charged, colourless or white. Free particles always exist in bound states and must have a colour charge of zero, because colour charged particles cannot be individually isolated. This phenomenon is called colour confinement and is a property of the strong force.

As previously mentioned, there are four known fundamental forces of nature: gravity, the electromagnetic, the weak and the strong force. So-called gauge bosons are the carriers of these fundamental forces. Gravity is described by general relativity and is not contained in the Standard Model of particle physics. It remains to be resolved how to merge these two theories in the future. So, beyond the Standard Model there are new gauge bosons needed. An example might be the graviton, which is a hypothetical particle and is supposed to be responsible for the gravitational force but could not yet be experimentally confirmed. Only the electromagnetic, the weak and the strong force are part of the Standard Model of particle physics. Every one of these three forces has a different number of force carriers, which means that there are in total 12 gauge bosons. Some of the basic properties of all four known fundamental forces of nature are listed in table 2 and ordered by their relative strength.

Table 2: The basic properties of the four fundamental forces of nature. The values for the relative strength are approximate figures for two fundamental particles at a constant distance from each other of 1 fm [3].

Fundamental force	Affected particles	Gauge boson	Mass (in GeV/c^2)	Spin	Relative strength
Strong	Hadrons	g	0	1	1
Electro-magnetic	Charged particles	γ	0	1	10^{-3}
Weak	Hadrons and leptons	$W^{\pm}$, Z^0	80.4, 91.2	1	10^{-8}
Gravity	All particles	Graviton?	0	2	10^{-37}

The strong force is the strongest one of all four fundamental forces of nature and is mediated by so-called gluons (g). It confines quarks into protons, neutrons and other hadrons and is responsible for the binding of nucleons in atomic nuclei. Furthermore, it is causing the binding of nucleons in atomic nuclei. In total, there are 8 gluons that always simultaneously carry a colour and an anticolour charge.

The weak force acts between all the fermions in the Standard Model of particle physics. Its interaction mechanism between subatomic particles participates in the weak decay of hadrons and is therefore responsible for the radioactive decay of atoms. Further information about the weak force will be given in section 2.2.2.

The electromagnetic force constitutes all the forces that are involved in the interaction between atoms. This is due to the fact that the electromagnetic force takes effect between the electrically charged atomic nuclei and electrons of the atoms. The resulting physical phenomena are light, electricity, magnetism, chemistry and several sorts of solid state properties.

2.2 V^0 particles and decays

2.2.1 Overview about V^0 decays

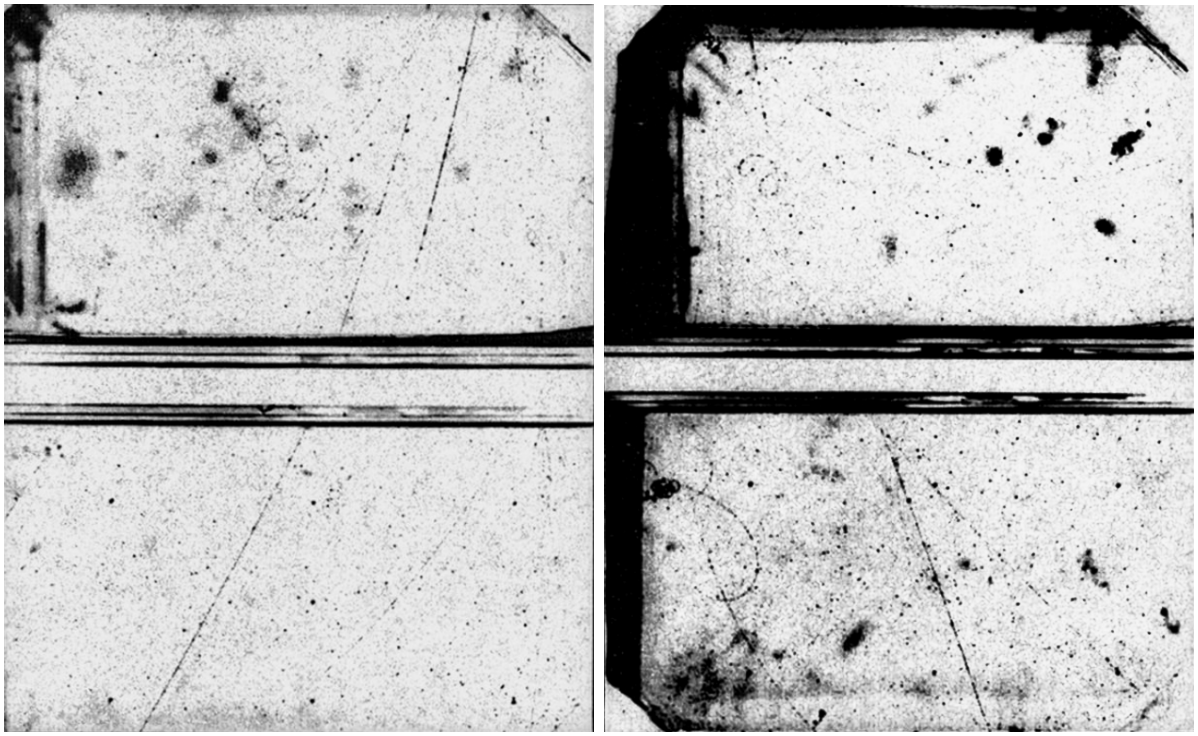

(a) "Example of a V^0 particle produced in a nuclear event in the lead blocks above the chambers. The decay track on the left corresponds to a negative particle, of momentum $(207 \pm 10)\,\mathrm{MeV}/c$, which is probably a π-meson. The decay track on the right corresponds to a positive particle, of momentum $(700 \pm 15)\,\mathrm{MeV}/c$, and is probably a proton, but in the lower chamber its ionisation and momentum indicate a somewhat lower mass. The energy release, assuming the products to be a π-meson and a proton, is $Q = (42 \pm 6)\,\mathrm{MeV}$." [4]

(b) "A V^0 decay which has a high Q-value. The decay occurs near the top center of the lower chamber. The positive particle is heavily ionising, and moves downward and slightly toward the right from the decay point, while the negative particle is near minimum ionisation and travels diagonally downward and to the right from the decay point. ... The Q-value calculated for this case is $(72 \pm 10)\,\mathrm{MeV}$." [4]

Figure 1: Two examples of V^0 decays visualised in a bubble chamber. The images are inverted to enhance the visibility of the tracks.

Nowadays, the term "V^0 particle" has fallen widely into disuse because by now all the related particles have been identified and given specific names. For instance, these

are kaons or lambda baryons. However, the naming still remains in some applications. So, dealing with V^0 particles arises the obvious question: What is a V^0 particle? V^0 particles are special heavy, unstable subatomic particles that decay into a pair of daughter particles. In a bubble chamber or in another kind of particle detector, the combined visible trajectories of these two daughter particles resemble a V-shaped form. Furthermore, V^0 particles are always neutrally charged. Both properties, the topology of the two decay products and the neutral charge, are responsible for the naming of V^0 particles [4]. For illustrative purposes, figure 1 shows two photos of a bubble chamber, where decays of V^0 particles are visible due to the appearance of two tracks at the same point.

Overall, four V^0 particles form the most common ones. First, there is the photon (γ). The second most common V^0 particle is the short-lived kaon (K_S^0). Lambda and antilambda baryons (Λ^0 and $\overline{\Lambda^0}$) form the third and fourth most common V^0 particles. Compared to the others, a photon does not decay weakly, so strictly speaking it is not a V^0 particle. Instead, it just converts into two new particles. However, from here on it is treated in the same way as the other V^0 particles because of its similar behaviour. On the one hand the utilised particle detector cannot directly observe the V^0 particles themselves because they tend to have a short life time, which is illustrated in table 3.

Table 3: Basic properties of the mother and the daughter particles in V^0 particle decays [5].

Particle	Rest mass (in MeV/c^2)	Mean life time τ (in s)	Approximate maximum range $c \cdot \tau$ (in cm)
Λ^0, $\overline{\Lambda^0}$	1115.683 ± 0.006	$(2.632 \pm 0.020) \times 10^{-10}$	7.89
K_S^0	497.611 ± 0.013	$(0.8954 \pm 0.0004) \times 10^{-10}$	2.68
γ	0	Varying	∞
p^+, p^-	$938.272 \pm 2.9 \times 10^{-7}$	Stable	∞
π^0	$134.977 \pm 5.0 \times 10^{-4}$	$(8.43 \pm 0.13) \times 10^{-17}$	2.53×10^{-6}
π^+, π^-	$139.570 \pm 1.8 \times 10^{-4}$	$(2.6033 \pm 0.0005) \times 10^{-8}$	7.80×10^2
e^-, e^+	$0.511 \pm 1.5 \times 10^{-10}$	Stable	∞

On the other hand the V^0 particles are neutrally charged and therefore do not interact electromagnetically. It is for these two reasons that one aims to detect the daughter

particles. Since they are charged and stable or at least long-living enough to hit the detector.

As shown in table 4, the lambda baryon primarily decays into a proton and a negative pion, while its antiparticle, the antilambda baryon, primarily decays into an antiproton and a positive pion.

Table 4: V^0 particles with their daughter particles and the daughters' daughter particles. Additionally, the two most dominant branching ratios of every particle are given [5].

Mother particle	Daughter particles and the two most dominant decays and their branching ratios	
Λ^0, $\overline{\Lambda^0}$	$p^+\pi^-$, $p^-\pi^+$ $(63.9 \pm 0.5)\,\%$	$n^0\pi^0$ $(35.8 \pm 0.5)\,\%$
K_S^0	$\pi^+\pi^-$ $(69.20 \pm 0.05)\,\%$	$\pi^0\pi^0$ $(30.69 \pm 0.05)\,\%$
γ	e^+e^- (in matter) $\approx 100.0\,\%$ (via pair production)	—
n^0	$p^+e^-\overline{\nu_e}$ $\approx 100.0\,\%$	—
π^0	$\gamma\gamma$ $(98.823 \pm 0.034)\,\%$	$e^+e^-\gamma$ $(1.174 \pm 0.035)\,\%$
π^+, π^-	$\mu^+\nu_\mu$, $\mu^-\overline{\nu_\mu}$ $(99.987\,70 \pm 0.000\,04)\,\%$	$e^+\nu_e$, $e^-\overline{\nu_e}$ $(1.230 \pm 0.004) \times 10^{-4}\,\%$

Short-lived kaons most likely decay into a positive and a negative pion. Looking at table 4, it becomes evident that there is more than one decay mode for short-lived kaons and lambda baryons. With branching ratios of $(30.69 \pm 0.05)\,\%$ and $(35.8 \pm 0.5)\,\%$, respectively, these decays include neutrons and neutral pions. However, neutrally charged particles are invisible in the detector so that the V^0 particle, which is in this case the short-lived kaon or the lambda baryon, cannot be analysed. Therefore, these two decay modes are not usable for the detection of V^0 particles. The photon almost exclusively converts into an electron and a positron via pair production. This process is elucidated

in section 2.2.3. Table 3 provides an overview of some of the properties of the mother and the daughter particles.

To bring V^0 particles into existence, there are several possible processes. One of them is to let a high-energy particle beam collide with a fixed target or another high-energy particle beam. These particles can be heavy ions like lead or gold. Protons are also a viable candidate for particles in a high-energy particle beam. In fact, this thesis also deals with proton-proton (pp) collisions. The interaction between the beam and the target, which can also be another beam, causes the emission of hadrons. So, this collision ultimately generates a bunch of particles but only the V^0 particles' daughter particles are detected. Lastly by applying appropriate cuts, the V^0 particles can be reconstructed. The collision is typically accompanied by gamma radiation and its interaction with matter is the cause for the appearance of electrons and positrons via pair production.

2.2.2 Weak interaction

Generally, there are some particles that decay by the weak force, which is also often called the weak interaction. Depending on the mediating gauge boson, one distinguishes between two different types of weak interaction. The $W^{\pm}$ bosons refer to the charged current interaction while the Z^0 boson refers to the neutral current interaction. Due to their significantly large mass of $m_{W^{\pm}} = (80.377 \pm 0.012)\,\mathrm{GeV}/c^2$ and $m_{Z^0} = (91.1876 \pm 0.0021)\,\mathrm{GeV}/c^2$, these force carriers are short-lived with a lifetime of under 10^{-24} seconds [5]. This causes the weak interaction to act only in short ranges.

The way bosons transfer charge to convert a neutral charge into a positive and a negative part, is an important mechanism for neutral V^0 particles. As they always decay into a positively and a negatively charged particle, it is the $W^{\pm}$ bosons and therefore the charged current interaction that is responsible for their decay. Besides the reaction equations of the V^0 particles, their decays can be illustrated in Feynman diagrams. Figure 2 shows the weak decays of K^0, $\overline{K^0}$, Λ^0 and $\overline{\Lambda^0}$.

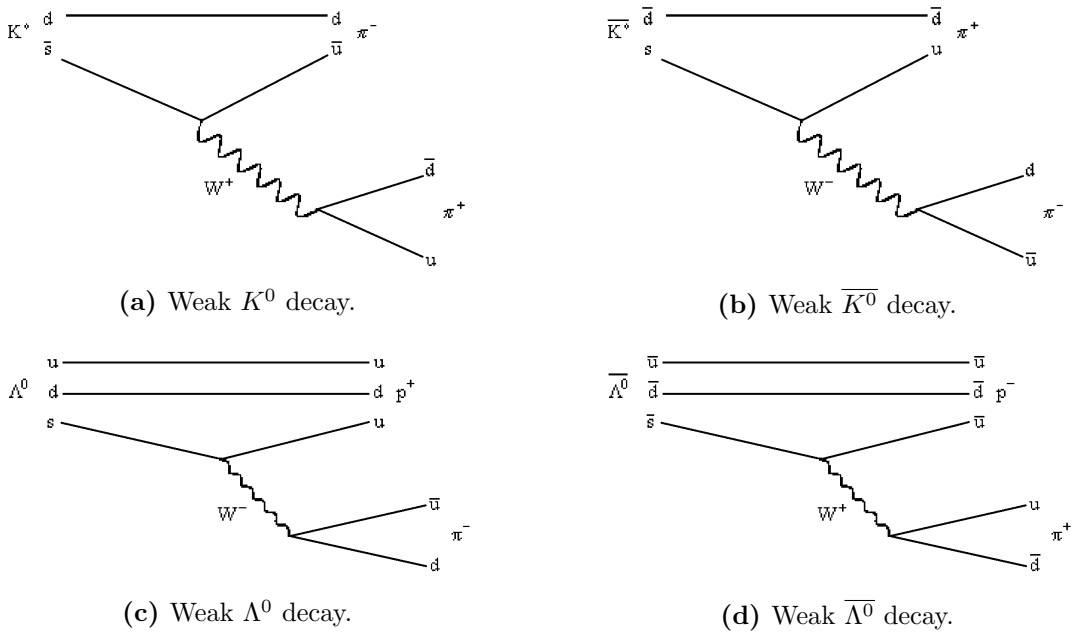

(a) Weak K^0 decay.

(b) Weak $\overline{K^0}$ decay.

(c) Weak Λ^0 decay.

(d) Weak $\overline{\Lambda^0}$ decay.

Figure 2: Weak decays of V^0 particles illustrated as Feynman diagrams.

Since the quark content of K^0_S is a mixture of K^0 ($d\bar{s}$) and $\overline{K^0}$ ($s\bar{d}$) states, it is their decay that is displayed in these Feynman diagrams.

The weak interaction is the only one that can change the flavour of quarks and leptons. This includes changing one type of quark into another. Due to the large masses of the $W^{\pm}$ bosons, quark transformations or decays that depend on the weak interaction typically occur significantly slower than transformations or decays that depend only on the strong or electromagnetic forces. Thus, V^0 particles have a relatively long life time compared to other unstable particles.

2.2.3 Pair production and photon conversion

Pair production is a process that turns a neutral boson into a particle and its antiparticle. The sum of flavour quantum numbers of this particle-antiparticle pair must be equal to zero. Since energy must be conserved as well, the necessary energy of the incoming mother boson must equal or exceed a threshold that corresponds to the sum of the rest mass energy of the two particles created. The most prominent pair production is the

conversion of a photon into an electron–positron pair. For this pair production to occur, the photon must be near a nucleus Z in order to satisfy conservation of momentum:

$$Z + \gamma \longrightarrow Z + e^- + e^+$$

As an electron–positron pair that is produced in free space cannot satisfy conservation of both energy and momentum [6]. Usually, what is relevant is the net reaction:

$$\gamma \longrightarrow e^- + e^+$$

So, the photon must reach an energy of at least 1022 keV while interacting with any material to create an electron–positron pair ($2 \cdot 511\,\mathrm{keV}$). Some part of the excessive energy converts into the electron's and positron's kinetic energy. The rest is given to the atomic nucleus, which receives some recoil.

The reverse process of the pair production is called annihilation. It occurs when a particle comes into contact with its antiparticle. In conformity with the previously mentioned photon conversion, the electron–positron annihilation shall serve here as an example:

$$e^- + e^+ \longrightarrow \gamma + \gamma$$

Conservation of energy and momentum are the principal constraints on both processes, pair production and annihilation.

2.3 Charmonium

In particle physics, a quarkonium is defined as a bound state which consists of a quark and its antiquark. This meson neither has a flavour nor an electric charge. Accordingly, a charmonium is a bound state of a charm quark (c) and a charm antiquark ($\overline{c}$). The J/ψ is the first charmonium that has been discovered. Furthermore, its discovery marks the first experimental observation of the fourth quark flavour, namely charm. This proved the existence of a fourth quark flavour and gave strong support to the quark model in general. The observation was announced simultaneously and independently by two research groups. At Brookhaven National Laboratory (BNL), a proton beam from the Alternating-Gradient Synchrotron collided with a beryllium target and a sharp mass peak was observed in the electron-positron channel [7]. Figure 3 shows the resulting invariant mass distribution of e^+e^- pairs in the relevant mass range.

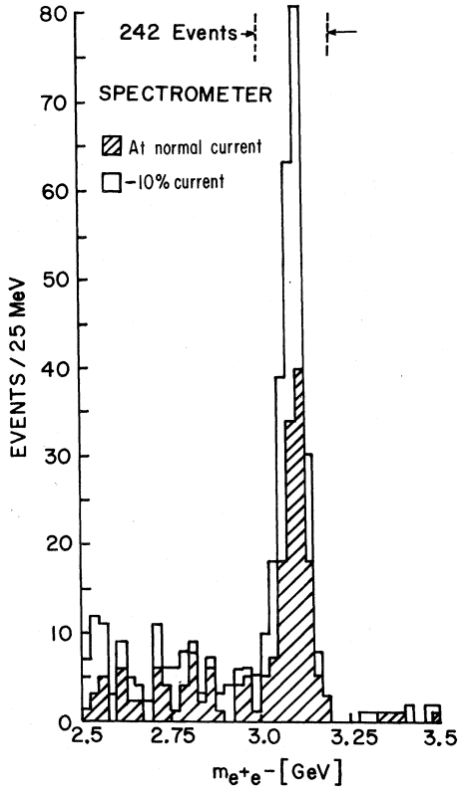

Figure 3: Invariant mass spectrum of e^+e^- pairs, which is recorded in p-Be collisions and showing the existence of the J/ψ meson [7].

Whereas at the Stanford Linear Accelerator Center (SLAC), a narrow resonance was observed in an electron-positron annihilation experiment in the SPEAR collider in hadronic and dileptonic channels [8]. The newly discovered particle was called J by the BNL group and ψ by the SLAC group. This led to the double name that it kept ever since.

The observed particle's narrow width of $\Gamma_{J/\psi} = (92.6 \pm 1.7)\,\mathrm{keV}/c^2$ explains its long lifetime and makes it the most durable $c\bar{c}$ among all charmonium states [5]. The $\Gamma_{J/\psi}$ value was also a strong sign for the fact that a new conserved quantum was at play. Being able to create the newly discovered state in electron-position annihilation led to the conclusion that the J/ψ must have the quantum numbers of the photon. It had to be a vector meson with $J^{PC} = 1^{--}$, which includes the total spin J, the parity quantum number $P = (-1)^{L+1}$ and the charge conjugation quantum number $C = (-1)^{L+S}$.

With $m_{J/\psi} = (3096.900 \pm 0.006)\,\mathrm{MeV}/c^2$ the mass of the J/ψ is below the open charm threshold, which is defined as twice the mass of the lightest open charm hadron ($2 \cdot m_{D^0} \approx 3728\,\mathrm{MeV}/c^2$) [5]. Therefore, the J/ψ cannot decay strongly into two D mesons. Due to the colour charge conservation, the decay into one gluon is not possible. It can also not decay into two gluons because the J/ψ possesses a negative C parity and a state of two gluons has a positive one. The first strong decay that is allowed proceeds via three virtual gluons. These gluons need to have high virtualities which means that the coupling at the strong interaction vertices is weak. As a consequence, the decay is suppressed. This mechanism is called OZI suppression [9][10][11] and leads to the fact that the electromagnetic decays into dileptons via a virtual photon become relevant:

$$J/\psi \longrightarrow e^+ + e^-$$
$$J/\psi \longrightarrow \mu^+ + \mu^-$$

Their branching ratios are $(5.971 \pm 0.032)\,\%$ and $(5.961 \pm 0.033)\,\%$, respectively [5].

Shortly after the discovery of the $J/\psi(1\mathrm{S})$, the radial excitation $\psi(2\mathrm{S})$ was observed. From the radiative decays between them that were discovered in e^+e^- storage rings

the existence of intermediate states with even C parity, namely the P-wave spin triplet $\chi_{cJ}(1P)$, was inferred. It was also derived that the spin singlet state $\eta_c(1S)$ with a mass below the J/ψ must exist. Later, the remaining charmonium states below the open charm threshold were identified. These are the radial excitation of the spin singlet state $\eta_c(2S)$ and the P-wave spin singlet state $h_c(1P)$. In addition, many more resonance particles have been found above the open charm threshold, some of which are of uncertain quark content and are candidates for exotic states. Figure 4 shows the different charmonium states with their masses and J^{PC} quantum numbers, the hadronic transitions between them and the different open charm thresholds.

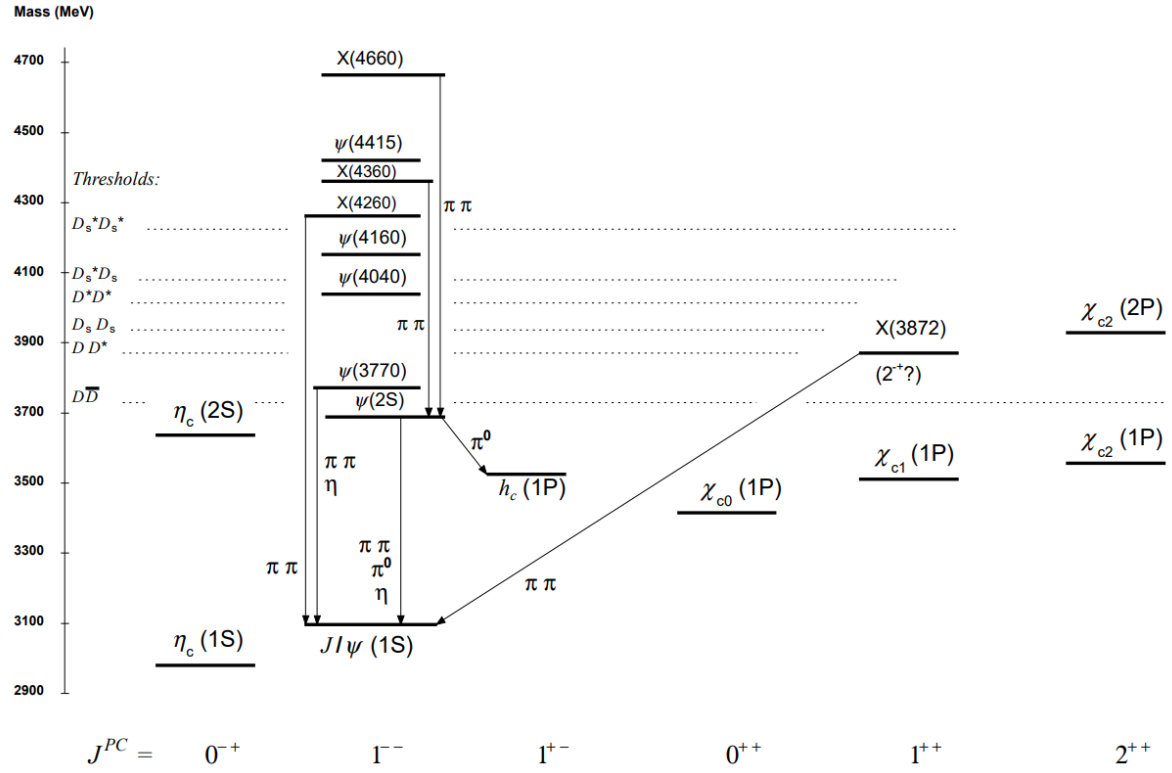

Figure 4: The level schema of the experimentally observed charmonium states. Observed hadronic transitions between the $c\bar{c}$ states as well as the mass thresholds for the decay to open charm mesons are also shown [12].

By looking at this level schema it becomes evident that the χ_c meson with $L = 1$ (1P) is not only one single particle. Instead, it is a spin triplet state including the χ_{c0}, the χ_{c1} and the χ_{c2}. Some of the basic properties of these three particles are listed in table 5.

Table 5: The basic properties of the charmonium states χ_{c0}, χ_{c1} and χ_{c2} [5].

Charmonium state	J^{PC}	Rest mass (in MeV/c^2)	Branching ratio of $\chi_{cJ} \to \gamma J/\psi$
χ_{c0}	0^{++}	3414.71 ± 0.30	$(1.40 \pm 0.05)\,\%$
χ_{c1}	1^{++}	3510.67 ± 0.05	$(34.3 \pm 1.0)\,\%$
χ_{c2}	2^{++}	3556.17 ± 0.07	$(19.0 \pm 0.5)\,\%$

Thereby one has to mention that the decay mode

$$\chi_{cJ} \longrightarrow \gamma + J/\psi$$

is the most dominant radiative decay for every χ_{cJ} state [5]. At the LHC at CERN a research group around the LHCb experiment measured the production of J/ψ and χ_c mesons in pp collisions at $\sqrt{s} = 7\,\text{TeV}$ [13]. While the J/ψ were reconstructed from the $\mu^+\mu^-$ decay channel, the χ_c were identified via the $\gamma J/\psi$ decay channel. The resulting invariant mass distribution of J/ψ as well as the $\Delta M = M(\mu^+\mu^-\gamma) - M(\mu^+\mu^-)$ distributions of χ_c for converted and non-converted photons are displayed in figure 5. In (a), (b) and (c) the background distribution is shown as a dashed purple curve. The solid red curve in (a) corresponds to the J/ψ signal. In (b) and (c) the upper solid blue curve belongs to the overall fit function, while the lower solid curves correspond to the fitted χ_{c0}, χ_{c1} and χ_{c2} contributions from left to right, respectively (the χ_{c0} peak is barely visible). The amplitude of these three peaks reflects the branching ratios of χ_{c0}, χ_{c1} and χ_{c2} in table 5. Thus, the χ_{c1} peak appears to be the most dominant one in the Δm spectrum.

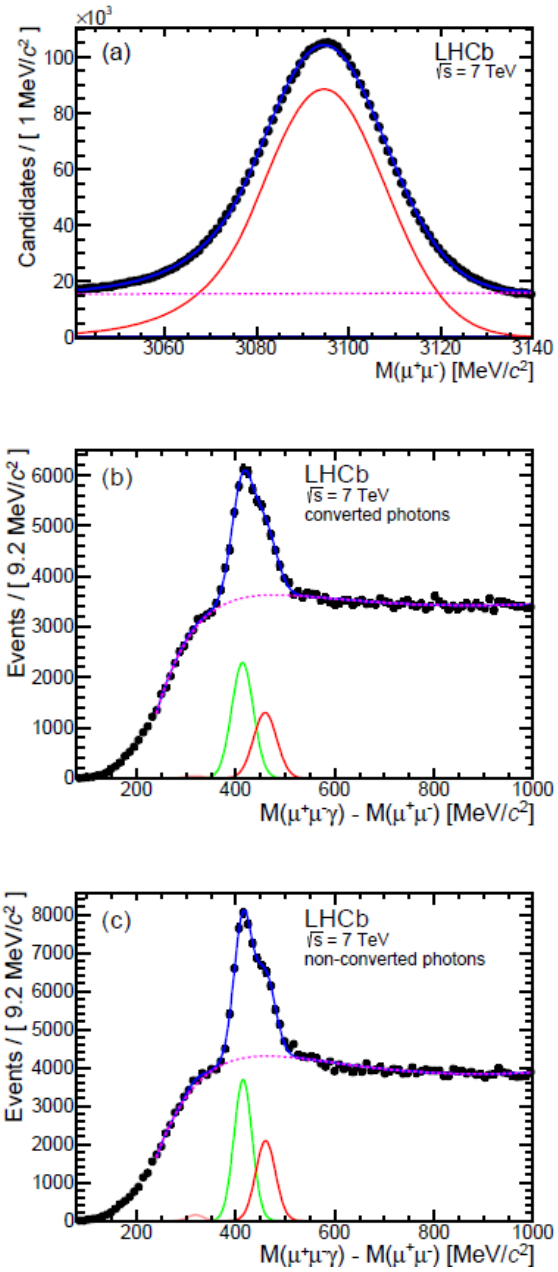

Figure 5: (a) Invariant mass distribution of the $\mu^+\mu^-$ pairs for selected J/ψ candidates. (b) and (c) show the $\Delta M = M(\mu^+\mu^-\gamma) - M(\mu^+\mu^-)$ distributions of selected χ_c candidates with converted and non-converted photons, respectively [13].

3 The ALICE Detector

In this part of the thesis the general setup of the experiment will be shown. Further, the steps performed to actually take the measurements in particular the particle detection will be discussed.

3.1 The ALICE Experiment at the LHC

3.1.1 The LHC at CERN

The Large Hadron Collider (LHC) [14] is located at the European Organization for Nuclear Research (CERN). It is the largest collider that has ever been built and reaches the highest collision energies. The crucial component is the ring collider, which is a synchrotron with a circumference of 26.7 km. It was built into the tunnel that was originally constructed for the Large Electron Positron Collider (LEP), 45 m to 170 m below the surface. An overview of the whole accelerator complex with its full pre-accelerator chain is given in figure 6.

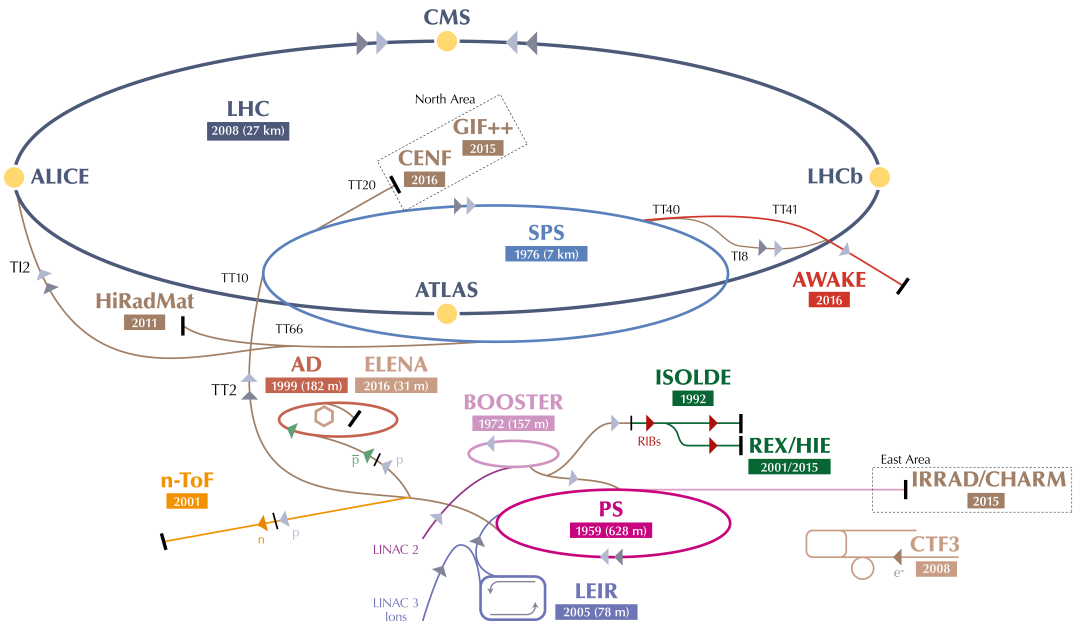

Figure 6: Schematic of the CERN accelerator complex and its four largest experiments [15].

Therein, the LHC is coloured in dark blue. As one can see, it forms the last ring in the complex chain of particle accelerators. These smaller accelerator machines are used in a chain to help boost the particles to their final energies and provide beams to a whole set of smaller experiments.

LHC's operation began in November 2009 and the Run-1 of data taking ended in February 2013. During this period the LHC delivered *pp* collisions at center-of-mass energies of up to $\sqrt{s} = 8\,\text{TeV}$, *p*-Pb collisions at $\sqrt{s_{NN}} = 5.02\,\text{TeV}$ and Pb-Pb collisions at $\sqrt{s_{NN}} = 2.76\,\text{TeV}$. After a two year maintenance and upgrade phase, which is called the Long Shutdown 1 (LS1), Run-2 started in April 2015. By this time, experiments were provided with *pp* collisions at $\sqrt{s} = 13\,\text{TeV}$, *p*-Pb collisions of up to $\sqrt{s_{NN}} = 8.16\,\text{TeV}$ and Pb-Pb collisions at $\sqrt{s_{NN}} = 5.02\,\text{TeV}$. There was also a new type of collision system introduced to the LHC: Xe-Xe collisions at $\sqrt{s_{NN}} = 5.44\,\text{TeV}$. Run-2 of data taking concluded in December 2018. Subsequent to a second maintenance and upgrade phase (LS2), which took over three years, Run-3 began in July 2022 and is currently operating. In this data taking period, the LHC is supposed to deliver *pp* collisions of up to $\sqrt{s} = 13.6\,\text{TeV}$.

There are seven experiments operating at the LHC. Four of them are large ones with a broad scientific scope. The three other experiments are smaller and more specialized, but they are located in the same caverns as the large experiments. In the following, all seven experiments will be listed.

ATLAS (A Toroidal LHC ApparatuS) [16] is the largest of all the LHC experiments and at the same time the largest detector that was ever built for particle physics. There are several cylindrical tracking and transition radiation layers that are positioned around the interaction point. They are complemented by calorimeters and muon spectrometers. ATLAS is a general purpose particle physics detector and searches for physical phenomena beyond the Standard Model, such as supersymmetry.

CMS (Compact Muon Solenoid) [17] is the second general purpose particle physics detector at the LHC. It is smaller but also heavier than ATLAS and has a different detector layout. Nevertheless, its physics goals are similar. The inner tracking and calorimeter layers of CMS are surrounded by a strong solenoidal magnet. Muon detectors

are placed outside of the magnet. They are nested in an iron structure. This so-called "return yoke" guides and contains the magnetic field.

ALICE (A Large Ion Collider Experiment) [18] is also a general purpose particle physics detector. It is dedicated to the study of heavy-ion collisions at the LHC. Section 3.1.2 will provide more details on this detector.

LHCb (Large Hadron Collider beauty) [19] has a main focus on heavy-flavour physics and in particular on CP violations. In contrast to the other large experiments, it is completely built at forward rapidity and uses high-precision tracking layers as well as various particle-identification techniques. The detector system offers the possibility to inject gas into the interaction region so that LHCb can be operated in a fixed-target mode and investigate cosmic ray physics.

TOTEM (Total Cross Section, Elastic Scattering and Diffraction Dissociation at the LHC) [20] is composed of several subdetectors that are located around the CMS detector at distances up to 217 m from the interaction vertex. Generally, it focuses on elastic proton collisions and diffractive processes but it also measures the total pp interaction cross section.

MoEDAL (Monopole and Exotics Detector at the LHC) [21] is placed around the intersection region of the LHCb detector. By using an array of plastic nuclear track detectors it searches for exotic phenomena such as magnetic monopoles, dysons and electrically-charged stable massive particles.

LHCf (Large Hadron Collider forward) [22] consist of two subdetectors. They are located at a distance of 140 m on either side of the ATLAS detector. In general, LHCf is designed for the measurement of neutral pions that are produced in the collisions at very forward regions. These neutral pions serve as an input to calibrate models of high energy cosmic rays.

3.1.2 ALICE Detector Layout

The ALICE detector [14] possesses some properties that are unique among the LHC experiments. On the one hand it provides a particle tracking ability that reaches down to

low transverse momenta. On the other hand ALICE is capable of particle identification in wide kinematic regions employing a broad range of different techniques. Figure 7 shows the schematic layout of the ALICE detector.

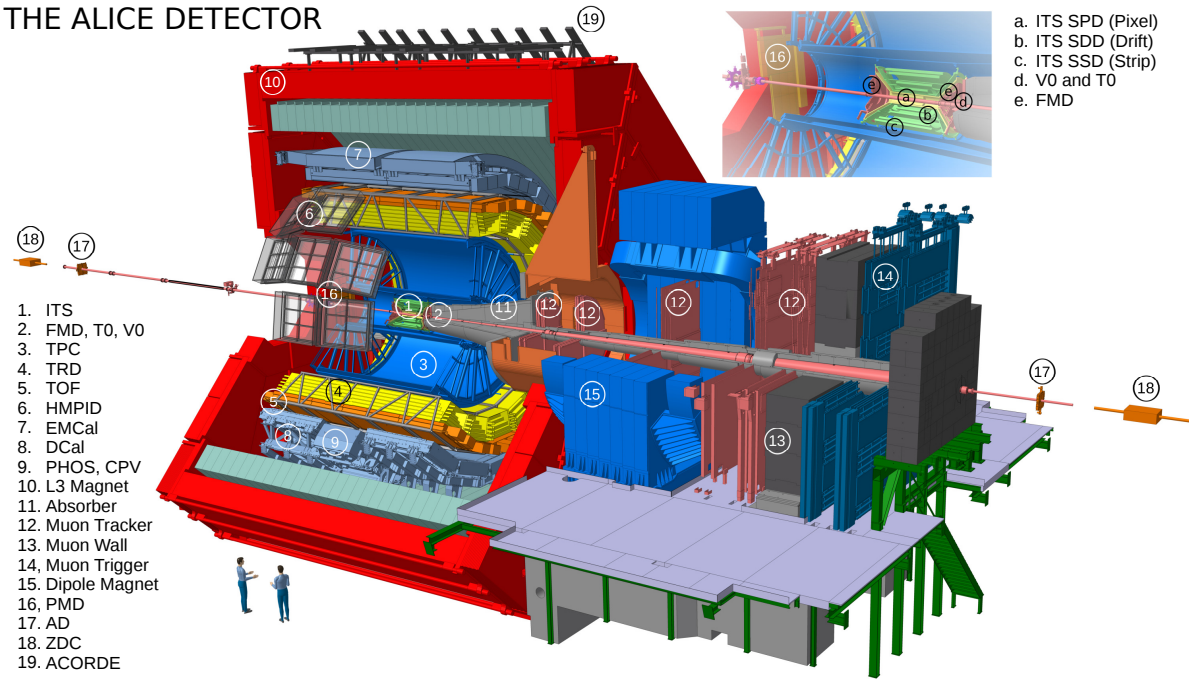

Figure 7: Three-dimensional schematic of the ALICE detector [23].

In the following the individual components of the ALICE detector are summarised shortly. The ones that are relevant for the analysis in this thesis will be further described in section 3.1.3, 3.1.4 and 3.1.5.

The main part of the ALICE detector is the large central barrel, which is built cylindrically around the interaction region. Closest to the interaction point is the ITS. It is surrounding the beam pipe and mainly responsible for the determination of the primary interaction vertex and secondary vertices. The TPC encases the ITS and forms the main tracking and PID device for the detector. On the outer edge of the TPC additional tracking and PID detectors are located. These are the TRD, the TOF, the EMCal, the DCal, the PHOS and the HMPID. The PMD is used as a photon multiplicity detector. There are several forward detectors inside of the central barrel that have specialized purposes. First, the T0

provides a trigger and an exact measurement of the time of collision. Second, the V0 is used for triggering, centrality determination in heavy-ion collisions and charged particle multiplicity determination at forward rapidity. In the latter purpose it is complemented by the FMD. Furthermore, the central barrel is encased by the L3 magnet. This is a huge solenoid that provides a homogeneous magnetic field of 0.5 T parallel to the beam axis forcing the outgoing charged particles on helical trajectories. On top of the L3 magnet lies the ACORDE subdetector that is responsible for the detection of high-momentum cosmic rays. The whole muon arm is a sequence of highly granular tracking planes and designed to detect muons. It is located in forward direction and behind a hadron absorber with a thickness of about 10 interaction lengths. A dipole magnet generates a field of 0.67 T. Behind an iron wall shielding of about 7.2 interaction lengths follows the muon trigger. The AD and the ZDC subdetectors are located further away from the main detectors. Both consist of two parts, which are placed on either side of the interaction point. The AD subdetectors are specialized in triggering on diffractive collisions and therefore they are positioned at very forward rapidities. In contrast, the ZDC subdetectors are located at even smaller angles to the beam and measure the energy of spectator nucleons. Thus, they serve as a centrality estimator in heavy-ion collisions.

3.1.3 The Inner Tracking System

The Inner Tracking System (ITS) [14] consists of six cylindrical silicon layers that employ three different technologies. All six layers cover the full azimuth, but different ranges in pseudorapidity.

The two innermost layers closest to the interaction point form the Silicon Pixel Detector (SPD). They are positioned at radii of 3.9 cm and 7.6 cm and cover a pseudorapidity range of $|\eta| < 2$ and $|\eta| < 1.4$, respectively. Both layers are composed of about 10 million hybrid silicon pixel cells with a size of 50 µm in $r\phi$ direction and 425 µm in z direction. The high granularity of the SPD and its proximity to the interaction point dominate the precision in the determination of the primary interaction vertex and secondary vertices from particle decays.

Due to the low material budget of about 1 % of a radiation length per layer, the tracking of low momentum particles down to approximately 80 MeV/c becomes possible. It also results in a low bremsstrahlung probability for electrons and a low pair production probability for photons. Both facts are advantageous for the reconstruction of J/ψ particles via the dielectron decay channel, which is in turn necessary for the analysis in this thesis. The information from the SPD detector can be used to estimate the charged particle multiplicity at midrapidity.

The third and fourth layer of the ITS are located at radii of 15 cm and 23.9 cm, respectively, and cover $|\eta| < 0.9$ both. They form the Silicon Drift Detector (SDD). It is responsible for providing highly granular tracking information in the drift and z direction.

The so-called Silicon Strip Detector (SSD) is composed of the last two ITS layers. They are positioned at radii of 38 cm and 43 cm, respectively, and cover $|\eta| < 0.98$ both. By acting together with the SDD, the SSD provides a specific energy loss signal $\frac{dE}{dx}$ that can be used for particle identification.

3.1.4 The V0 Detector

The V0 system [14] consists of two scintillator arrays on either side of the interaction point. On the one hand the V0A that is placed 329 cm from the nominal vertex and covers a pseudorapidity range of $2.8 < \eta < 5.1$. On the other hand the V0C that is located on the front face of the hadron absorber between 86 cm and 88 cm from the nominal vertex and covers a pseudorapidity range of $-3.7 < \eta < -1.7$. Each one of these scintillator arrays is segmented in four rings in radial direction and eight sectors in azimuthal direction. In total, there are $2 \times 4 \times 8$ channels. Each of them is composed of a plastic scintillator that is connected to a photomultiplier tube via wavelength shifting fibers.

The V0 can be used to provide a trigger signal for data taking. For the analysis in this thesis, the minimum bias trigger is of particular significance. This type of trigger consists of a coincidence signal from both aforementioned V0 arrays. The V0 is also capable of providing a so-called high-multiplicity trigger, which requires a deposited energy above a

given threshold in the system. Depending on the chosen trigger, collisions are selected or rejected.

In addition, the V0 can be used to reject background from interactions between the beam and the residual gas in the beam pipe as well as from interactions between the beam halo and various accelerator components. Moreover, based on the energy deposited in the scintillators, the charged particle multiplicity at forward rapidity can be estimated.

3.1.5 The Time Projection Chamber

The Time Projection Chamber (TPC) [14] is the main tracking and particle identification device of the ALICE detector. It provides a three dimensional reconstruction of charged particle tracks. The TPC is shaped like a hollow cylinder with an inner radius of 84.8 cm, an outer radius of 246.6 cm and a length in beam direction of 499.4 cm. With these dimensions, it covers the full azimuth and $|\eta| < 0.9$ for tracks crossing the full radial length of the detector. However, at higher pseudorapidities of up to $|\eta| < 1.5$ some tracks still cross parts of the detector and can be reconstructed with $\frac{1}{3}$ radial length. The central high voltage cathode is responsible for dividing the active volume of the TPC into two halves. It is set to a voltage of -100 kV and provides a homogeneous electric drift field of 400 V/cm along the beam direction.

The aforementioned active volume is filled with a gas mixture of Ar and CO_2. If charged particles traverse, they will ionise this gas. The electrons that thus become free drift along the electric field and move towards the two end caps on either side of the TPC. Collisions with the gas molecules compensate the acceleration that is generated by the electric field, so the electrons receive a constant drift velocity of 2.65 cm/µs. This leads to a resulting maximum drift time of 94 µs. The ions drift in the opposite direction but their velocity is about a factor of 1000 smaller.

The end caps of the TPC are segmented in 18 sectors in azimuthal direction. Each sector is equipped with two multiwire proportional chambers (MWPC) with cathode pad readout, ordered in radial direction, the inner and outer readout chambers (IROC and OROC). These chambers are divided into pads with sizes between $4 \times 7.5\,\mathrm{mm}^2$ and $6 \times 15\,\mathrm{mm}^2$ depending on their radial position. In total, there are 278 784 pads on either

side of the TPC that are arranged in 159 rows in radial direction. Due to the constant drift velocity of the electrons, their arrival time can be translated into the z coordinate of their creation with 1000 samples in this direction. This leads to a number of 557 million voxels in space that can be used to reconstruct the three dimensional trajectory of a particles.

From the radius of the curvature in the constant magnetic field one can extract the momentum of the traversing particles. Their specific energy loss per path length $\frac{dE}{dx}$, which depends on their velocity β, is measured from the deposited charge in the readout pads. By combining these two informations, the mass of the particle can be determined. Hence, the particle can be identified. More details on particle identification will be given in section 3.2.

3.2 Particle Identification

3.2.1 Tracking

Generally, there are several steps that take part in the ALICE central barrel tracking and vertex finding procedure. Figure 8 shows these steps schematically as a flow chart.

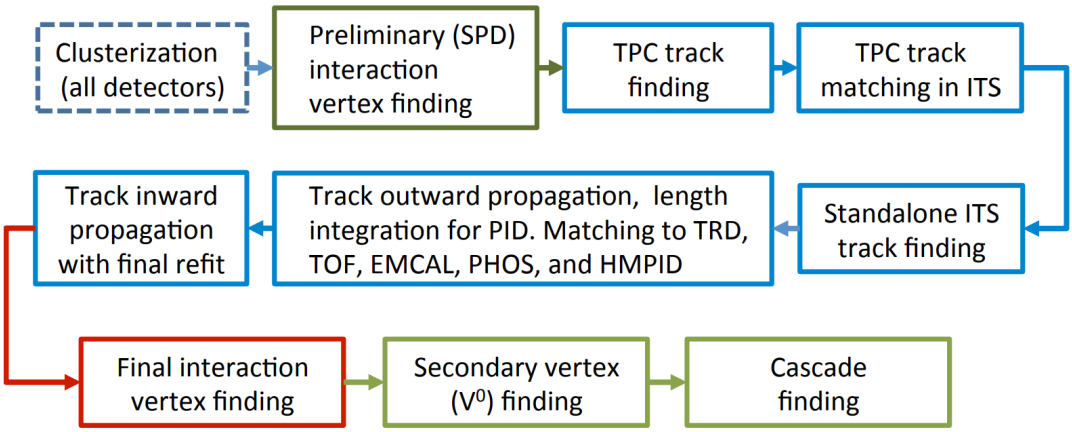

Figure 8: Flow chart of the central barrel event reconstruction in ALICE [24].

Here, a short summary of the individual steps will be given. Further information about them can be found in [24].

Clusterization is the first step, which is done individually for every detector. The detector signals are merged into clusters based on their position in space and time. From the clusters in the SPD, a preliminary interaction vertex is constructed. To achieve this, tracklets are constructed as lines that are defined by pairs of clusters in the first and second SPD layer and a point of convergence for a maximum number of tracklets is searched. This procedure is repeated various times in order to find additional interaction vertices of pileup events. The next step is the track finding and fitting. This is a three stages process that follows an inward-outward-inward scheme. It starts by combining clusters in the outermost regions of the TPC to track seeds. This seeding is done twice, once with taking the information of the interaction vertex into account and once without. A so-called Kalman filter approach is utilised by adding clusters compatible with the estimated track parameters, so that the track seeds are propagated inward towards the inner TPC wall. In doing so, one has to ensure that not too many seeds use the same clusters. Based on the specific energy loss $\frac{dE}{dx}$ in the TPC, a preliminary PID hypothesis is set. The assumed mass is necessary to correct the energy loss of the particle that traverses the gas. In the next step, the reconstructed TPC tracks are propagated to the outermost ITS layer and become the seeds for the track finding in the ITS. The seeding is proceeded again once with and once without the information on the primary vertex. By taking shared clusters and dead zones of the detector into account, the seeds are propagated inwards. Afterwards a standalone ITS tracking is performed with clusters that were not used for the ITS–TPC tracks. This is due to the reduced tracking efficiency in the TPC at low transverse momenta. Subsequently, the tracks are propagated outwards by starting from the point of closest approach to the preliminary interaction vertex. By matching to the detectors at larger radii than the TPC, the TRD, the TOF, the EMCal, the PHOS and the HMPID are attempted. The third and last stage of tracking is the propagation back inwards. It starts from the outer wall of the TPC. By using the previously found clusters, the tracks are refitted in the TPC and the ITS. The final values of the track parameters and the corresponding covariance matrices are obtained. Afterwards, by using the combined ITS-TPC tracks, a final interaction vertex is determined, which has a higher precision than the preliminary one that was only created from the SPD

tracklets.

During the tracking procedure, kink, V^0 and cascade topologies are investigated and the tracks belonging to them are flagged accordingly. The kink topology consists of an incoming and an outgoing track. They are called the kink mother and the kink daughter, respectively. Essentially, the kink daughter continues outward under some finite angle to the kink mother. They are typically produced by charged particles that decay weakly into a charged and a neutral particle, for instance $K^+ \rightarrow \mu^+ + \nu_\mu$. The V^0 topology is composed of two outgoing tracks that have the closest approach to each other at some secondary vertex distinct from the interaction vertex. As described in section 2.2, they are produced either by photon conversion to electron-positron pairs in the detector material or by neutral particles decaying into two charged particles, for example $K^0_S \rightarrow \pi^+ + \pi^-$. Further information on the V^0 topology will be given in section 3.2.2. Cascades are more complicated topologies that are originating from a cascading decay chain of charged and neutral particles. For instance, the decay $\Xi^- \rightarrow \Lambda^0 + \pi^-$ is followed by $\Lambda^0 \rightarrow p^+ + \pi^-$.

Lastly, the particle identification (PID) in ALICE is achieved with different subdetectors and by employing various techniques. These will be briefly summarised in the following. More details are given in [24].

The ITS provides an ionisation energy loss signal from its four outer layers [14]. By normalising the path length, a $\frac{dE}{dx}$ value can be obtained from every layer. This value is used to calculate a truncated mean. As a consequence, the highest charge clusters are discarded. In particular, it is a helpful tool in low momentum region where the ITS is used for standalone tracking.

The TRD (Transition Radiation Detector) is responsible for particle identification based on the specific energy loss and transition radiation (TR) of traversing particles [14]. TR will be emitted by relativistic particles, if they traverse the interface of two materials with different dielectric constant. The onset of TR is at around $\beta\gamma = \frac{p}{m} > 1000$. As a result, electrons with momenta above $p > 0.5\,\mathrm{GeV}/c$ emit TR, while hadrons do not up to much higher momenta. Thus, TR can be used to distinguish electrons from hadrons. The TRD covers the full central barrel acceptance and has a six layer structure. Every layer is composed of a radiator followed by a drift chamber, which is filled with a gas mixture of

Xe and CO_2. The radiator consists of polypropylene fiber mats that are wedged between two Rohacell foam sheets. Incoming TR photons deposit energy in the gas of the drift chamber and end up being absorbed. Particle identification can be obtained either solely from the deposited energy or by also taking the time dependence of the energy loss into account. The TRD can also be used as a physics trigger on high-momentum electrons, jets and nuclei.

The TOF (Time-Of-Flight) detector is capable of identifying particles by measuring the time interval they need to travel a defined distance [14]. For this a start time is necessary, which is provided by the T0 detector. The T0 is composed of two arrays of Cherenkov counters on either side of the interaction point. The TOF itself consists of multigap resistive plate chamber. It covers the full central barrel acceptance and can measure the arrival time of particles with a resolution of about 80 ps. In combination with the momentum information from the tracking detectors, the TOF allows particle identification in the intermediate momentum range. So, kaons and pions can be detected up to $p = 2.5\,\mathrm{GeV}/c$ and protons can be observed up to $p = 4\,\mathrm{GeV}/c$.

The EMCal (ElectroMagnetic Calorimeter), the DCal (Di-Jet Calorimeter) and the PHOS (Photon Spectrometer) are electromagnetic calorimeters. They are ideal for the identification of electrons [14]. Since electrons deposit their entire energy in an electromagnetic calorimeter, while hadrons typically only lose a small fraction. In combination with momentum measured by the tracking detectors, the fraction of deposited energy in the calorimeters can be determined. Hence, the electrons can be distinguished from the hadrons. All three electromagnetic calorimeters cover limited acceptance in pseudorapidity and azimuth. By serving as an extension of the EMCal, the DCal enables the study of hadron-jet and di-jet correlations. Furthermore, the three detectors can also provide triggers on high momentum electrons or photons.

The HMPID (High Momentum Particle Identification Detector) is a ring-imaging Chrenkov detector [14]. It is responsible for the separation of hadrons up to high momenta. Thus, kaons an be distinguished from pions up to $p_T = 3\,\mathrm{GeV}/c$ and protons up to $p_T = 5\,\mathrm{GeV}/c$. Only 5 % of the acceptance of the central barrel is covered by the HMPID.

The TPC provides particle identification that is based on the simultaneous measurement of the specific energy loss $\frac{dE}{dx}$ and the rigidity R (momentum divided by charge) of each track [14]. For a given material and in first leading-order, the energy loss depends on the charge, the velocity β and the Lorentz factor γ. It can be described with the Bethe-Bloch curve. In the TPC the energy loss is measured in up to 159 samples from the single readout pad rows. A truncated mean is calculated from these individual values. The velocity dependence can be parametrized with the formula

$$f(\beta\gamma) = \frac{P_0}{\beta^{P_3}} \left[P_1 - \beta^{P_3} - \ln\left(P_2 + \frac{1}{(\beta\gamma)^{P_4}} \right) \right] \tag{3.1}$$

which includes the relativistic particle velocity β, the Lorentz factor γ and the fit parameters $P_0, \ldots, P_4$. Figure 9 shows the experimentally obtained $\frac{dE}{dx}$ values as a function of the particle momentum.

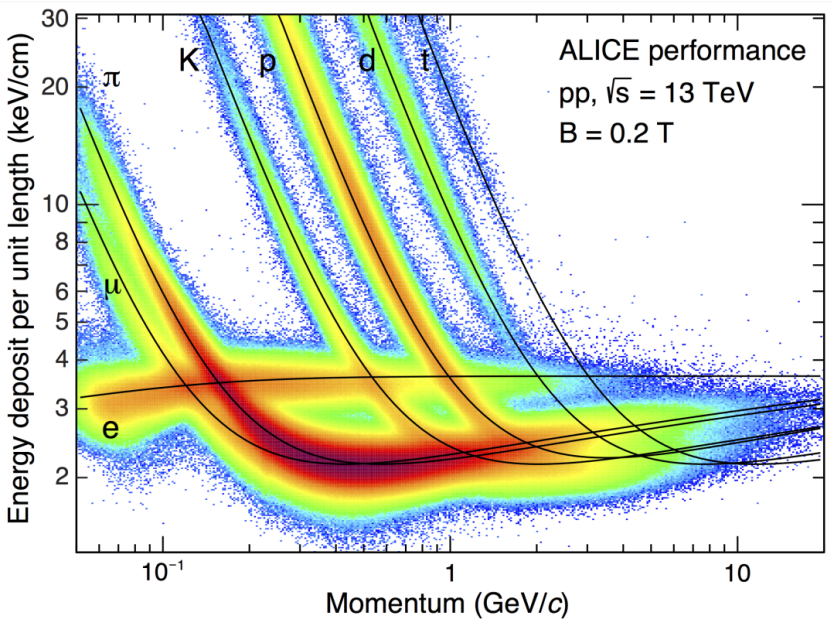

Figure 9: Specific energy loss $\frac{dE}{dx}$ in the TPC versus particle momentum in *pp* collisions at $\sqrt{s}13\,\text{TeV}$. The lines show the parametrizations of the expected mean energy loss for different particle species [25].

The energy loss for various particles that is expected from the parametrized Bethe-Bloch curve is illustrated as well. A clear separation between the particle species in wide momentum regions is visible. There are also regions of overlapping between them. At high momentum the curves merge and an identification is no longer possible for individual tracks. However, some particle abundances can still be determined on a statistical basis by using Gaussian fits to the energy loss in slices of momentum. The resolution of $\frac{dE}{dx}$ is around 5.2 % and the distribution at a given $\beta\gamma$ and particle species is Gaussian down to at least three orders of magnitude. This means that the width of the distributions can be quantified with the standard deviation σ. Typically, the variable $n\sigma_{\mathrm{TPC},i}$ is used, which is the deviation of the measured energy loss to the expected energy loss of a certain particle species $i \in \{e^{\pm}, \pi^{\pm}, p^{\pm}\}$ divided by the width σ_i of the distribution for this particle species:

$$n\sigma_{\mathrm{TPC},i} = \frac{\left(\frac{dE}{dx}\right)_{\mathrm{measured}} - \left(\frac{dE}{dx}\right)_{\mathrm{expected},i}}{\sigma_i} \tag{3.2}$$

The expected energy loss and the width are corrected for each track and for additional detector effects depending on the pseudorapidity and the number of TPC clusters that were used for PID.

3.2.2 V^0 Detection

The particle identification of the daughter particles of the V^0 decays is important for several applications [26]. Therefore, it is necessary to obtain a truly pure sample of protons, electrons, pions and their corresponding antiparticles. For instance, these particles can also be used for calibration purposes. To gain pure particles, the PID software has to analyse the detected particles with respect to certain properties.

The reconstruction of the tracks of the V^0 particles' daughter particles is already a part of the identification and was discussed in section 3.2.1. Essentially, the resulting tracks are put together considering different conditions and by cutting on the following values that must be calculated beforehand. First, the distance of the daughter tracks to the

primary vertex. Second, the distance of closest approach (DCA) between the daughter tracks. The pointing angle θ is also a main quantity. As the momentum of the mother particle should point to the primary vertex. Lastly, a causality check is performed. This means that the absence of space points in forbidden ITS layers can be required if the decay takes place far enough from the vertex. Figure 10 displays the topology of a V^0 decay with its main variables.

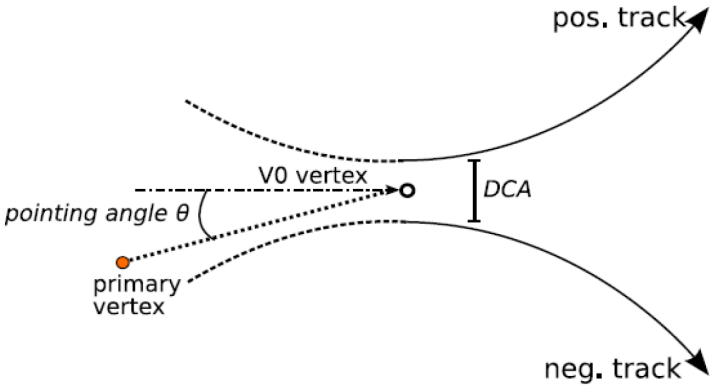

Figure 10: General topology of a V^0 decay [26].

Generally speaking, there are two types of vertices. On the one hand the event vertex or primary vertex. This is the location where two accelerated high energy protons or heavy ions collide. As a result, the primary vertex is the origin of new particles that come into existence. On the other hand the secondary vertex or V^0 vertex is the location where unstable particles, which arise from the collision or another process, decay into new particles. A photon's point of conversion into an electron-positron pair is also considered as a secondary vertex.

The straight line between the primary vertex and the V^0 vertex and the reconstructed mother track define the pointing angle θ. This variable is also illustrated in figure 10.

In V^0 decays two decisive angles are defined: ξ_{Pair} and Ψ_{Pair}. Both angles can be seen in figure 11.

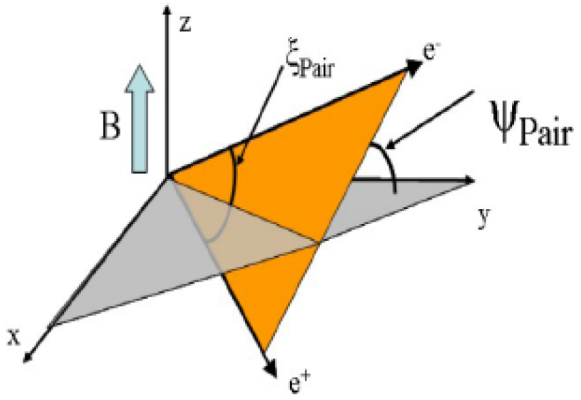

Figure 11: Illustration of the angles ξ_{Pair} and Ψ_{Pair}. An electron and a positron serve as an example [26].

ξ_{Pair} is the angle between the daughter tracks and is given by

$$\xi_{\text{Pair}} = \arccos\left(\frac{\vec{p_{i^-}} \cdot \vec{p_{i^+}}}{||\vec{p_{i^-}}|| \cdot ||\vec{p_{i^+}}||}\right) \tag{3.3}$$

where $i^{\pm}$ is the negative and the positive daughter particle, respectively. In addition, $\vec{p_{i^{\pm}}}$ is the corresponding momentum. Ψ_{Pair} is the angle between the plane that the daughter tracks span and the plane that is orthogonal to the magnetic field. It is defined as

$$\Psi_{\text{Pair}} = \arcsin\left(\frac{\Delta\vartheta_0}{\xi_{\text{Pair}}}\right) \tag{3.4}$$

Thereby, $\Delta\vartheta_0$ is the difference between the angles of the two daughter particles in regard to the magnetic field direction $\vec{z}$:

$$\Delta\vartheta_0 = \left|\vartheta_0(i^-) - \vartheta_0(i^+)\right| \tag{3.5}$$

The relativistic energy-momentum relation of a single particle is defined as

$$E^2 = m^2c^4 + p^2c^2 \tag{3.6}$$

which includes the energy E, the mass m, the momentum p and the speed of light in vacuum c. In an isolated system the total energy and momentum of all particles remain constant at any time. Naturally, this is also valid for a two-body decay process. Hence, the so-called centre-of-mass energy or invariant mass M of a decay into two particles is given by the Mandelstam variable s:

$$s = M^2 = (E_1 + E_2)^2 - (\vec{p_1} + \vec{p_2})^2 \tag{3.7}$$

Here, E_1 belongs to the first and E_2 to the second daughter particle. $\vec{p_1}$ and $\vec{p_2}$ are the three-momentum vectors of the first and the second daughter particle, respectively.

In probability theory and statistics the quantity χ^2 is used. One can hypothesise and assign a certain mother particle to a vertex. In fact, it is measurable how likely it is that this hypothesis is true. The higher the calculated χ^2 value, the lower is the probability. Another parameter is the number of degrees of freedom (NDF), which is the number of parameters that are free to vary. Typically, NDF is 3. While performing the identification of V^0 particles, there is a maximal accepted value for $\frac{\chi^2}{\mathrm{NDF}}$. All higher $\frac{\chi^2}{\mathrm{NDF}}$ values are omitted. Often, $\frac{\chi^2}{\mathrm{NDF}}$ is called reduced χ^2.

4 Data analysis

In this section the reconstruction of χ_c mesons from *pp* collisions at the LHC is performed. First, some general information and descriptions will be given. Afterwards the individual steps of the analysis procedure will be presented.

For the analysis Run-2 ESD data from 2016 is processed. This includes the periods LHC16d, LHC16e, LHC16g, LHC16h, LHC16i, LHC16j, LHC16o, LHC16p, LHC16l and LHC16k. In total, there are over 630 million events analysed, which are originating from *pp* collisions in the ALICE detector at a centre-of-mass energy of $\sqrt{s} = 13\,\mathrm{TeV}/c$. All these events are detected by using a minimum bias (MB) trigger. To facilitate the analysis the reducedTree framework [27] is utilised. It contains a large set of analysis tools to be used in particle physics and is currently focused mainly on ALICE Collaboration analysis.

As mentioned in section 2.3, $\chi_c \to \gamma + J/\psi$ is the most probable radiative decay of a χ_c meson. Using this $\gamma J/\psi$ decay channel to reconstruct χ_c, one has to put J/ψ and photons together. While creating the J/ψ from the e^+e^- decay channel, the photons are handled as V^0 particles. The principle behind this is described in section 2.2. Photons are the only V^0 particles that will be used in this analysis. To extract any particle signal from the recorded data, a variety of cuts needs to be applied. Initially, the appropriate events must be filtered and thus event cuts are necessary. They are shown in table 6.

Table 6: Event cuts and their selection criteria.

Quantity	Selection criterion
Minimum vertex contributors	1
Primary vertex z_{Vtx}	$-10\,\mathrm{cm} < z_{\mathrm{Vtx}} < 10\,\mathrm{cm}$
Physics selection	Required

For the reconstruction of J/ψ, electrons and positrons are used. As mentioned in section 3.2.1, they form tracks in the detector. To filter them, a first set of track cuts and track prefilter cuts is applied during the creation of the minimum biased data. This marks the

first round of filtering. These loose track cuts and track prefilter cuts are shown in table 7 and 8.

Table 7: Track cuts and their selection criteria in the first round of filtering.

Quantity	Selection criterion
p_{IN}	$1\,\mathrm{GeV}/c < p < 1 \times 10^{30}\,\mathrm{GeV}/c$
Pseudorapidity η	$-0.9 < \eta < 0.9$
Impact parameter (transverse direction) DCA_{xy}	$-1\,\mathrm{cm} < \mathrm{DCA}_{xy} < 1\,\mathrm{cm}$
Impact parameter (longitudinal direction) DCA_z	$-3\,\mathrm{cm} < \mathrm{DCA}_z < 3\,\mathrm{cm}$
ITS tracking quality	$0 < \frac{\chi^2}{N_{\mathrm{cls.ITS}}} < 50$
TPC tracking quality	$0 < \frac{\chi^2}{N_{\mathrm{cls.TPC}}} < 4$
Number of TPC clusters	$50 < N_{\mathrm{cls.TPC}} < 161$
TPC electron inclusion	$-4 < n\sigma_{\mathrm{TPC},e} < 4$
TPC proton exclusion	$1 < n\sigma_{\mathrm{TPC},p} < 1 \times 10^{20}$
TPC pion exclusion	$1 < n\sigma_{\mathrm{TPC},\pi} < 1 \times 10^{20}$
ITS refit	Required
TPC refit	Required

Table 8: Track prefilter cuts and their selection criteria in the first round of filtering.

Quantity	Selection criterion
Momentum p	$0.5\,\mathrm{GeV}/c < p < 1 \times 10^{30}\,\mathrm{GeV}/c$
Pseudorapidity η	$-2 < \eta < 2$
Impact parameter (transverse direction) DCA_{xy}	$-2\,\mathrm{cm} < \mathrm{DCA}_{xy} < 2\,\mathrm{cm}$
Impact parameter (longitudinal direction) DCA_z	$-3\,\mathrm{cm} < \mathrm{DCA}_z < 3\,\mathrm{cm}$
TPC electron inclusion	$-3 < n\sigma_{\mathrm{TPC},e} < 3$
TPC kaon inclusion	$-2 < n\sigma_{\mathrm{TPC},K} < 2$
TPC proton inclusion	$-2 < n\sigma_{\mathrm{TPC},p} < 2$
ITS refit	Required
TPC refit	Required

In a second round of filtering, far stricter track cuts and track prefilter cuts are applied.

These so-called standard track cuts for the analysis of J/ψ production are necessary for the J/ψ signal extraction and background reduction. They are listed in table 9 and 10.

Table 9: Track cuts and their selection criteria in the second round of filtering.

Quantity	Selection criterion
Momentum p	$1\,\mathrm{GeV}/c < p < 30\,\mathrm{GeV}/c$
Pseudorapidity η	$-0.9 < \eta < 0.9$
Impact parameter (transverse direction) DCA_{xy}	$-1\,\mathrm{cm} < \mathrm{DCA}_{xy} < 1\,\mathrm{cm}$
Impact parameter (longitudinal direction) DCA_z	$-3\,\mathrm{cm} < \mathrm{DCA}_z < 3\,\mathrm{cm}$
TPC tracking quality	$0 < \frac{\chi^2}{N_{\mathrm{cls.TPC}}} < 4$
Number of TPC clusters	$70 < N_{\mathrm{cls.TPC}} < 160$
TPC electron inclusion	$-3 < n\sigma_{\mathrm{TPC},e} < 3$
TPC proton exclusion	$3 < n\sigma_{\mathrm{TPC},p} < 3 \times 10^4$
TPC pion exclusion	$3 < n\sigma_{\mathrm{TPC},\pi} < 3 \times 10^4$
Kink topologies	Daughters rejected
ITS refit	Required
TPC refit	Required
Hit in SPD	Required in at least one layer

Table 10: Track prefilter cuts and their selection criteria in the second round of filtering.

Quantity	Selection criterion
Momentum p	$0.7\,\mathrm{GeV}/c < p < 100\,\mathrm{GeV}/c$
TPC refit	Required

It should be noted, that the track prefilter cuts in the second round of filtering are an additional set of cuts especially to obtain low momentum electrons and positrons. This allows the pairing of lower momentum tracks with higher momentum tracks, which is ultimately raising the J/ψ candidate yield. Table 11 shows a set of pair cuts that are also used.

Table 11: Pair cuts and their selection criteria in the second round of filtering.

Quantity	Selection criterion
Transverse momentum p_T	$0\,\mathrm{GeV}/c < p_T < 100\,\mathrm{GeV}/c$
Rapidity y	$-0.9 < y < 0.9$

The cuts for the V^0 particles are also applied during the creation of the minimum biased data. However, unlike in the case of the tracks, there is no second round of filtering. As a prefilter function for all V^0 particle candidates, the Armenteros-Podolanski plot is used. In this special two-dimensional plot, the transverse momentum Q_T of the positive daughter particle with respect to the reconstructed mother particle's momentum is plotted against the longitudinal momentum asymmetry α. Thus, the kinematic properties of the V^0 particles are illustrated. An example can be seen in figure 12a.

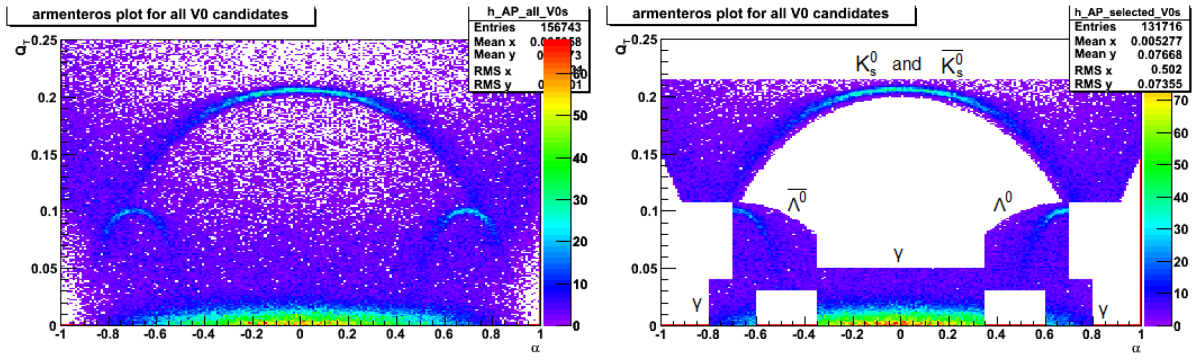

(a) Armenteros-Podolanski plot without any cuts. **(b)** Armenteros-Podolanski plot with applied cuts.

Figure 12: Armenteros-Podolanski plots for all detected V^0 particle candidates. (a) and (b) have a number of 500 and 700 entries, respectively. Every sliced area in (b) can be associated to a certain type of V^0 particle. These cuts are fixed values and cannot be changed [26].

Generally, in the Armenteros-Podolanski plot, there are areas that correspond to certain types of V^0 particles. These areas can be cut out, which ultimately results in Q_T and α cuts for V^0 particle candidates. This is shown in figure 12b. More details on Armenteros-Podolanski plots in the context of V^0 particle identification can be found in [26]. Furthermore, there are plenty of cuts for the V^0 particles' daughter particles. Since photons are the only V^0 particles that are relevant for the analysis in this thesis,

the cuts displayed in table 12 and 13 correspond to the main contributors of the photon conversion process.

Table 12: Cuts for the selection of electrons and positrons from photon conversion.

Quantity	Selection criterion
Number of TPC clusters	$50 < N_{\text{cls.TPC}} < 160$
TPC refit	Required
TPC tracking quality	$0 < \frac{\chi^2}{N_{\text{cls.TPC}}} < 4$
TPC cluster ratio	> 0.6
Kink topologies	Daughters rejected
TPC electron inclusion	$-3 < n\sigma_{\text{TPC},e} < 3$
Momentum p	$0.2\,\text{GeV}/c < p < 1 \times 10^{30}\,\text{GeV}/c$
Pseudorapidity η	$-1.2 < \eta < 1.2$
ITS refit	Required

Table 13: Cuts for the selection of photon conversion. One has to point out, that these are loose cuts, which differ from the default cuts mentioned in [26].

Quantity	Selection criterion
Reduced χ^2	$\frac{\chi^2}{\text{NDF}} < 10$
Pointing angle θ	$0\,\text{rad} < \theta < 0.05\,\text{rad}$
DCA of the two daughter tracks	$0\,\text{cm} < \text{DCA} < 1\,\text{cm}$
Radius r of the secondary vertex	$3\,\text{cm} < r < 90\,\text{cm}$
Ψ_{Pair}	$0\,\text{rad} < \Psi_{\text{Pair}} < 0.2\,\text{rad}$
Invariant mass M	$0\,\text{GeV}/c^2 < M < 0.1\,\text{GeV}/c^2$

Table 12 is a list of cuts that are applied to filter electrons and positrons originating solely from photon conversion. By combining their tracks, photons are assembled with respect to the cuts in table 13.

The first step of the analysis is the reconstruction of J/ψ, which is performed in the following way. In every event the negative tracks from electrons are paired randomly with the positive tracks from positrons. As a result, J/ψ candidates with several attributes

are formed. The most important attributes are the energy E, the invariant mass $m_{e^+e^-}$, the three-momentum vector $\vec{p}$, the transverse momentum p_T, the pseudorapidity η and the azimuth angle ϕ. While E and $m_{e^+e^-}$ are calculated using equation 3.6 and 3.7, $\vec{p}$ is estimated by adding the electron's three-momentum vector component-wise to the positron's three-momentum vector. By employing

$$p_x = p_T \cos(\phi) \tag{4.1}$$

$$p_y = p_T \sin(\phi) \tag{4.2}$$

$$p_z = p_T \sinh(\eta) \tag{4.3}$$

$$|\vec{p}| = p_T \cosh(\eta) \tag{4.4}$$

the other attributes can be converted into one another. The invariant mass distribution of the resulting J/ψ candidates in the relevant $m_{e^+e^-}$ range is illustrated in figure 13a.

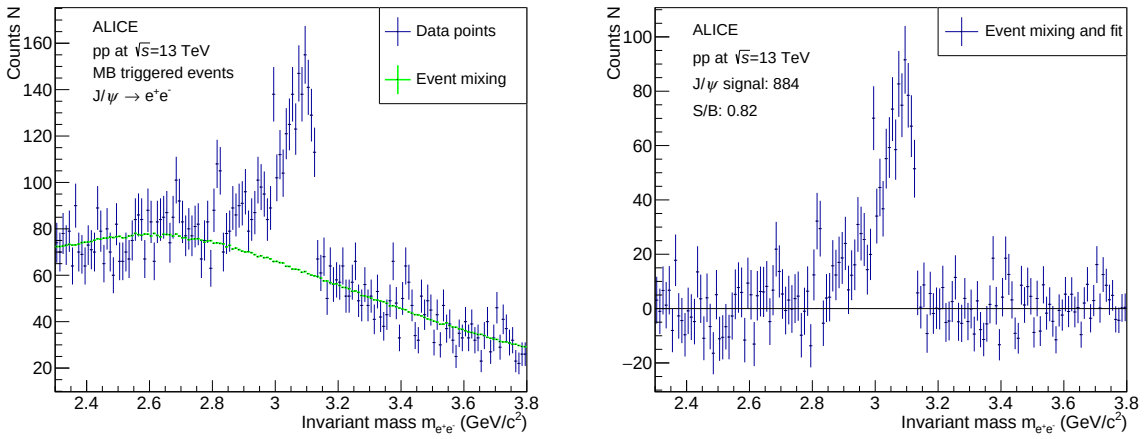

(a) Invariant mass distribution of the reconstructed J/ψ candidates.

(b) Extracted J/ψ signal after the background reduction.

Figure 13: The initial (a) and the processed (b) invariant mass distributions of the reconstructed J/ψ candidates.

Additionally, the invariant mass distribution of the event mixing is shown, which is scaled and normalised by the range of 2.2 GeV/c^2 to 2.8 GeV/c^2. It is provided to describe the

background. In figure 13a, a peak is readily visible. By knowing the mass of the J/ψ from section 2.3, it is evident that this peak corresponds to the J/ψ meson. To reduce the background, a signal extraction of the J/ψ signal is performed. Firstly, the invariant mass distribution of the event mixing is subtracted from the invariant mass distribution of the J/ψ candidates. Since the event mixing is partly overestimating the background, further actions are necessary. In order to gain a suitable fit for the remaining background, one has to cut out the J/ψ peak in the range of $2.87\,\mathrm{GeV}/c^2$ to $3.2\,\mathrm{GeV}/c^2$. The utilised fit function is a second-order polynomial. Lastly, both background descriptions, namely the invariant mass distribution of the event mixing and the obtained background fit, are subtracted from the initial invariant mass distribution of the J/ψ candidates. The resulting histogram with the extracted J/ψ signal is displayed in figure 13b. Now, by summing up the entries between $2.99\,\mathrm{GeV}/c^2$ and $3.16\,\mathrm{GeV}/c^2$, the number of observed J/ψ can be estimated. This J/ψ signal and its signal-to-background ratio $\frac{S}{B}$ are included in figure 13b.

In the next step of the analysis, the focus is on the photons. Generally, the analysis software differentiates between offline and on the fly V^0 particles. So, photons are classified accordingly. On the one hand offline V^0 particles are found based on reconstructed tracks and have a high level of abstraction. This means that they run on ESD tracks. They can also be replayed and reconfigured at will. Their disadvantage is an inadequate resolution because of the cluster association before the decay point. On the other hand on the fly V^0 particles are found during tracking in the cluster. Since the raw cluster is used, an optimal resolution is provided and there are no clusters before the decay point. The fact that on the fly V^0 particles can only be replayed and reconfigured little to nothing at analysis level is disadvantageous. In this analysis, offline and on the fly photons are used but it has to be mentioned that both types of photons must be treated separately from each other. Photons are massless by definition. Although photons are massless by definition, there are some photons in the data that possess a mass. This is partly because of numerical discrepancies in the analysis software. However, the masses of the photons are still relatively low, not least because of the cut in the invariant mass that is specified in table 13. Therefore, it is the photons' momentum p that plays the largest part in the photons' contribution to the invariant mass of the reconstructed χ_c candidates. Figure 14 shows the momentum and transverse momentum distributions of the photons that are

used in this analysis.

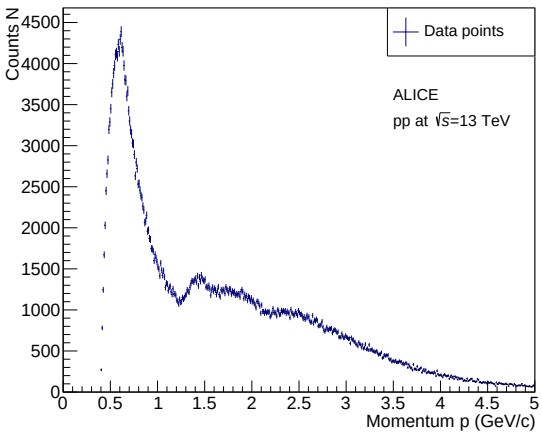

(a) Offline photons.

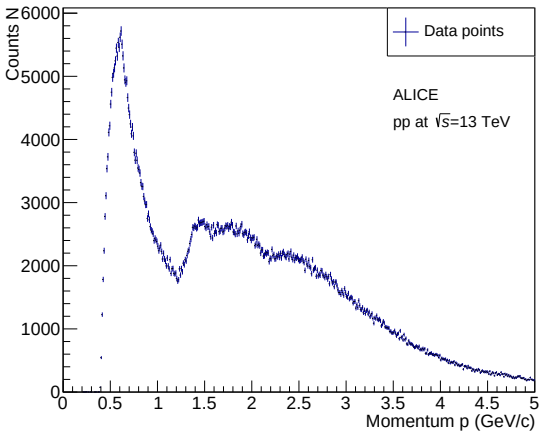

(b) On the fly photons.

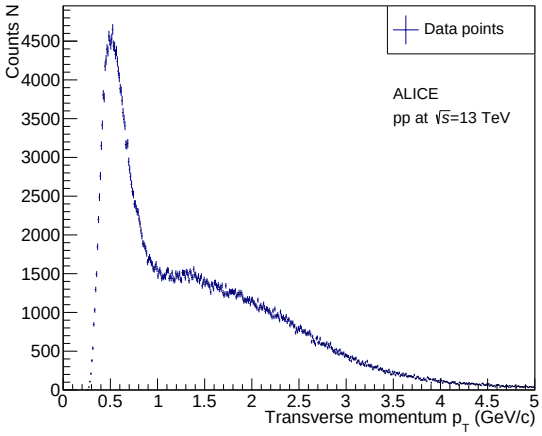

(c) Offline photons.

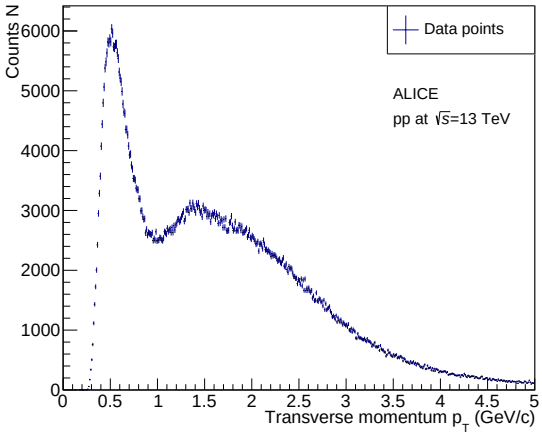

(d) On the fly photons.

Figure 14: The momentum and transverse momentum distributions for offline and on the fly photons.

In particular, low momentum photons are necessary for the χ_c analysis because the mass difference of $\Delta m = \left| m_{\chi_c} - m_{J/\psi} \right| \approx 0.4\,\mathrm{GeV}/c^2$ can be associated to the photon that also takes part in the $\chi_c \to \gamma + J/\psi$ decay. The photon carries this Δm in the form of energy and momentum. In figure 14a and 14b, it can be seen that the lowest momentum of the

photons is at around $0.4\,\mathrm{GeV}/c$, which is due to the momentum cut for electrons and positrons in table 12.

In the following the creation of neutral pions π^0 will be performed. The reason behind this is to provide a checking for the photons. As specified in table 3, the neutral pion decay $\pi^0 \to \gamma + \gamma$ is electromagnetic with a branching ratio of almost 100 %. Thus, π^0 can be constructed using the $\gamma\gamma$ decay channel. The objective is to observe a peak with a significant amplitude. This peak is supposed to be situated at the π^0 rest mass of $m_{\pi^0} = (134.977 \pm 5.0 \times 10^{-4})\,\mathrm{MeV/c^2}$ in the invariant mass distribution of the reconstructed π^0 candidates. The pairing of the photons is very similar to the pairing of the tracks in the reconstruction of J/ψ: For every event photons are paired randomly. Thereby, one has to pay attention and prevent the photons from pairing with themselves. Just like the J/ψ candidates, the resulting π^0 candidates possess multiple attributes naturally including the invariant mass $m_{\gamma\gamma}$. The calculations are done in the same manner as for the J/ψ candidates. Figure 15 illustrates the invariant mass distributions of the reconstructed π^0 candidates in the relevant $m_{\gamma\gamma}$ range.

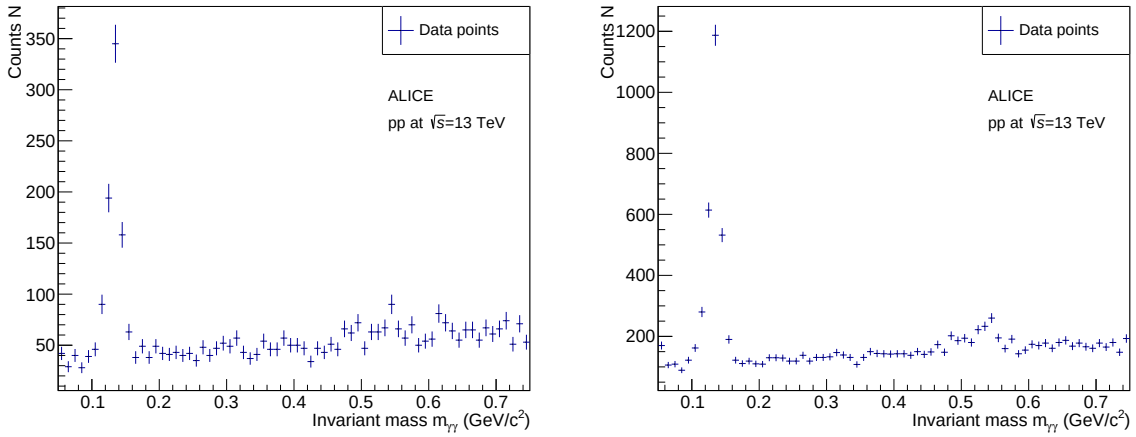

(a) Created with offline photons. **(b)** Created with on the fly photons.

Figure 15: Invariant mass distributions of the reconstructed π^0 candidates.

The π^0 peak at around $140\,\mathrm{MeV}/c^2$ is very readily visible in both histograms. In addition, the glimpse of another peak can be discovered at $m_{\gamma\gamma} \approx 550\,\mathrm{MeV}/c^2$. This peak belongs presumably to the η meson because it has a mass of $(547.862 \pm 0.017)\,\mathrm{MeV}/c^2$ and decays

into two photons with a branching ratio of $(39.36 \pm 0.18)\,\%$ [5]. Evidently, one can say that the photons are appropriate for the χ_c analysis.

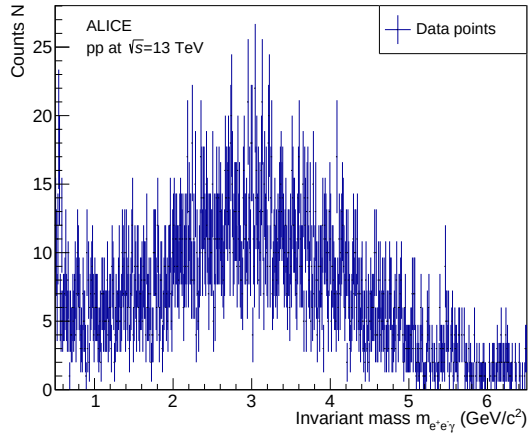

(a) Created with offline photons and without a J/ψ mass cut.

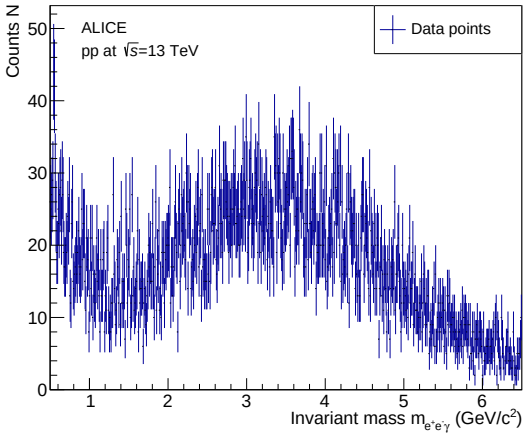

(b) Created with on the fly photons and without a J/ψ mass cut.

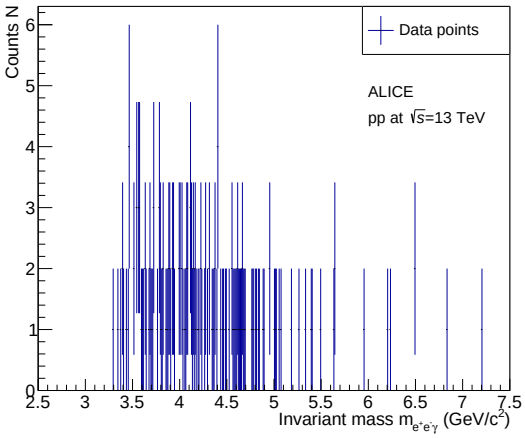

(c) Created with offline photons and a J/ψ mass cut.

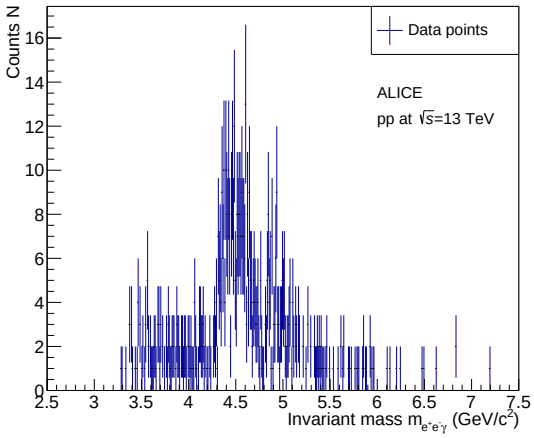

(d) Created with on the fly photons and a J/ψ mass cut.

Figure 16: Invariant mass distributions of the reconstructed χ_c candidates. (a) and (c) are created with offline photons, (b) and (d) with on the fly photons. For the distributions in (c) and (d), a cut in the invariant mass of the J/ψ candidates is applied, which is $2.92\,\mathrm{GeV}/c^2 \leq m_{e^+e^-} \leq 3.16\,\mathrm{GeV}/c^2$.

The last step of the analysis is the actual reconstruction of χ_c. This is accomplished by using all J/ψ candidates that were created previously in this analysis. Since the

all photons turn out to be appropriate for the analysis, there are no further photon cuts necessary. The event-wise, random pairing of the photons with the J/ψ candidates is performed following the same principle that was already presented for the creation of J/ψ and π^0 candidates. As a result, χ_c candidates with a variety of attributes are formed. This also includes the invariant mass $m_{e^+e^-\gamma}$. Figure 16a and 16b show the resulting invariant mass distributions of the reconstructed χ_c candidates. Additionally, the pairing of the photons with the J/ψ candidates is processed once again but this time a cut of $2.92\,\mathrm{GeV}/c^2 \leq m_{e^+e^-} \leq 3.16\,\mathrm{GeV}/c^2$ in the invariant mass of the J/ψ candidates is applied. The range of this cut differs from the invariant mass range that was used to extract the J/ψ signal. This is because the J/ψ candidates' background was not reduced before employing them again in the χ_c reconstruction. Figure 16c and 16d display the resulting invariant mass distributions of the reconstructed χ_c candidates with an applied J/ψ mass cut. By looking at these two figures, there cannot be any significant information gathered because the number of entries is not high enough. In figure 16a and 16b, there is no peak visible that can be associated to one of the χ_{cJ} states mentioned in section 2.3. Even the χ_{c1} state that is supposed to generate the most dominant peak in the invariant mass distribution is not observable. Hence, the χ_c signal cannot be distinguished from the background.

5 Conclusions

In this section previous results are summed up and discussed in more depth.

First of all, the obtained J/ψ signal is evaluated. The successful background reduction in the invariant mass distribution of the reconstructed J/ψ candidates in figure 13 leads to a total number of 884 observed J/ψ. By knowing that over 630 million minimum biased events are analysed, one can estimate that in this analysis 1.4 J/ψ per million events are obtained. This is in agreement with the rough estimation of 2 J/ψ per million events, which are expected for minimum biased data and standard track cuts. The signal-to-background ratio of $\frac{S}{B} = 0.82$ speaks in favour of the ALICE detection efficiency.

The photons turn out to be ideal for the χ_c analysis. Their momentum and transverse momentum reaches down to under $0.4\,\mathrm{GeV}/c$, which is low enough to let the photons become potential contributors in the $\chi_c \to \gamma + J/\psi$ decay. Additionally, they fulfil the characteristics that one would expect from photons created as a consequence of high energy pp collisions. As it is possible to use the photons for the construction of neutral pions.

For the χ_c reconstruction it was expected to observe a peak for each of the three χ_{cJ} states in the invariant mass distributions of the reconstructed χ_c candidates in figure 16, as described in section 2.3. The most significant peak, namely the one from the χ_{c1} state, was supposed to be located at around $m_{\chi_{c1}} = (3.510\,67 \pm 0.000\,05)\,\mathrm{GeV}/c^2$ [5].

In reality, there is not a single χ_{cJ} peak in the invariant mass distributions. Instead, one only observes background. This means that the χ_c signal is too low to be distinguished from the background. Not even the cut in the invariant mass of the J/ψ candidates can provide an increased resolution. Instead, it lowers the number of entries in the histogram and restrains the appearance of low mass χ_c candidates, which can be seen in figure 16c and 16d.

In fact, there are several reasons for the vanishing of the χ_c signal in the background. Firstly, the photons that originate evidently from pi^0 and η are not filtered out. Furthermore, an adequate background reduction is lacking. In general, there are not enough

events being processed in this analysis. Thus, the χ_c reconstruction is limited in statistics. However, one can roughly estimate how many events are necessary to detect one χ_c. Starting with the sufficient assumption that 30 % of the 884 obtained J/ψ are from χ_c decays. The probability to detect the photon from the $\chi_c \to \gamma + J/\psi$ decay can be roughly estimated as 10 %. This is the conversion probability that depends on the cuts for the selection of electrons and positrons from photon conversion. Its exact value can only be determined via Monte Carlo simulations. So, $30\,\% \cdot 884 \approx 265$ J/ψ are coming from the χ_c decays. From these 265 J/ψ, 10 % of the photons originating from the χ_c decays can be detected. In total, roughly $10\,\% \cdot 30\,\% \cdot 884 \approx 27$ χ_c are observed in the over 630 million minimum biased events. This leads to an approximate number of 24 million events that need to be analysed to obtain one χ_c. Nonetheless, this is only a rough estimation that is severely associated with the transverse momentum of the photons and their cut in momentum. Thus, the number of 24 million events for one χ_c is difficult to handle.

To enhance the χ_c signal, one could attempt different variations of cuts. Moreover, the aforementioned photons that originate evidently from π^0 and η could be filtered out by applying a new cut and tagging them accordingly. Main part of the issue is that more data is required. Perhaps it should be considered to expand the data sample to the periods LHC17 and LHC18. Run-3 of data taking would also provide more data.

References

[1] CERN. *Physics*. 2022. URL: https://home.web.cern.ch/science/physics (visited on 09/18/2022).

[2] Juan Knaster, R Veness, and L Gamez-Mejias. "The vacuum chamber in the interaction region of particle colliders: a historical study and developments implementations in the LHCb experiment at CERN". In: (Jan. 2004), p. 2.

[3] Mark Thomson. *Modern particle physics*. Cambridge University Press, 2013.

[4] R. B. Leighton, S. D. Wanlass, and C. D. Anderson. "The Decay of V^0 Particles". In: *Phys. Rev.* 89 (1 Jan. 1953), pp. 148–167. DOI: 10.1103/PhysRev.89.148. URL: https://link.aps.org/doi/10.1103/PhysRev.89.148.

[5] R. L. Workman et al. "Review of Particle Physics". In: *PTEP* 2022 (2022), p. 083C01. DOI: 10.1093/ptep/ptac097.

[6] J.H. Hubbell. "Electron–positron pair production by photons: A historical overview". In: *Radiation Physics and Chemistry* 75.6 (2006). Pair Production, pp. 614–623. ISSN: 0969-806X. DOI: https://doi.org/10.1016/j.radphyschem.2005.10.008. URL: https://www.sciencedirect.com/science/article/pii/S0969806X0500263X.

[7] J. J. Aubert et al. "Experimental Observation of a Heavy Particle J". In: *Phys. Rev. Lett.* 33 (23 Dec. 1974), pp. 1404–1406. DOI: 10.1103/PhysRevLett.33.1404. URL: https://link.aps.org/doi/10.1103/PhysRevLett.33.1404.

[8] J. -E. Augustin et al. "Discovery of a Narrow Resonance in e^+e^- Annihilation". In: *Phys. Rev. Lett.* 33 (23 Dec. 1974), pp. 1406–1408. DOI: 10.1103/PhysRevLett.33.1406. URL: https://link.aps.org/doi/10.1103/PhysRevLett.33.1406.

[9] S. Okubo. "Φ-meson and unitary symmetry model". In: *Physics Letters* 5.2 (1963), pp. 165–168. ISSN: 0031-9163. DOI: https://doi.org/10.1016/S0375-9601(63)92548-9. URL: https://www.sciencedirect.com/science/article/pii/S0375960163925489.

[10] G Zweig. *An SU_3 model for strong interaction symmetry and its breaking; Version 1*. Tech. rep. Geneva: CERN, 1964. URL: https://cds.cern.ch/record/352337.

[11] Jugoro Iizuka. "A Systematics and Phenomenology of Meson Family*". In: *Progress of Theoretical Physics Supplement* 37-38 (Mar. 1966), pp. 21–34. ISSN: 0375-9687. DOI: 10.1143/PTPS.37.21. eprint: https://academic.oup.com/ptps/article-pdf/doi/10.1143/PTPS.37.21/5215468/37-38-21.pdf. URL: https://doi.org/10.1143/PTPS.37.21.

[12] J. Beringer et al. "Review of Particle Physics". In: *Phys. Rev. D* 86 (1 July 2012), p. 010001. DOI: 10.1103/PhysRevD.86.010001. URL: https://link.aps.org/doi/10.1103/PhysRevD.86.010001.

[13] R. Aaij et al. "Measurement of the ratio of prompt χ_c to J/ψ production in pp collisions at $\sqrt{s} = 7\,\text{TeV}$". In: *Physics Letters B* 718.2 (2012), pp. 431–440. ISSN: 0370-2693. DOI: https://doi.org/10.1016/j.physletb.2012.10.068. URL: https://www.sciencedirect.com/science/article/pii/S0370269312011343.

[14] Steffen Georg Weber. "Multiplicity dependent J/ψ production in proton-proton collisions at the LHC". en. PhD thesis. Darmstadt: Technische Universität, Oct. 2018. URL: http://tuprints.ulb.tu-darmstadt.de/8461/.

[15] Esma Mobs. "The CERN accelerator complex. Complexe des accélérateurs du CERN". In: (2016). General Photo. URL: http://cds.cern.ch/record/2197559.

[16] The ATLAS Collaboration et al. "The ATLAS Experiment at the CERN Large Hadron Collider". In: *Journal of Instrumentation* 3.08 (Aug. 2008), S08003–S08003. DOI: 10.1088/1748-0221/3/08/s08003. URL: https://doi.org/10.1088/1748-0221/3/08/s08003.

[17] The CMS Collaboration et al. "The CMS experiment at the CERN LHC". In: *Journal of Instrumentation* 3.08 (Aug. 2008), S08004–S08004. DOI: 10.1088/1748-0221/3/08/s08004. URL: https://doi.org/10.1088/1748-0221/3/08/s08004.

[18] K. Aamodt et al. "The ALICE experiment at the CERN LHC". In: *JINST* 3 (2008), S08002. DOI: 10.1088/1748-0221/3/08/S08002.

[19] The LHCb Collaboration et al. "The LHCb Detector at the LHC". In: *Journal of Instrumentation* 3.08 (Aug. 2008), S08005–S08005. DOI: 10.1088/1748-0221/3/08/s08005. URL: https://doi.org/10.1088/1748-0221/3/08/s08005.

[20] G. Antchev et al. "The TOTEM detector at LHC". In: *Nucl. Instrum. Meth. A* 617 (2010). Ed. by Giorgio Chiarelli et al., pp. 62–66. DOI: 10.1016/j.nima.2009.08.083.

[21] James Pinfold et al. *Technical Design Report of the MoEDAL Experiment*. Tech. rep. 2009. URL: https://cds.cern.ch/record/1181486.

[22] The LHCf Collaboration et al. "The LHCf detector at the CERN Large Hadron Collider". In: *Journal of Instrumentation* 3.08 (Aug. 2008), S08006–S08006. DOI: 10.1088/1748-0221/3/08/s08006. URL: https://doi.org/10.1088/1748-0221/3/08/s08006.

[23] Arturo Tauro. "ALICE Schematics". General Photo. 2017. URL: https://cds.cern.ch/record/2263642.

[24] "Performance of the ALICE experiment at the CERN LHC". In: *International Journal of Modern Physics A* 29.24 (Sept. 2014), p. 1430044. DOI: 10.1142/s0217751x14300440. URL: https://doi.org/10.1142%2Fs0217751x14300440.

[25] "First results of the ALICE detector performance at 13 TeV". In: (2015). URL: https://cds.cern.ch/record/2047855.

[26] David Baumeier. "V0 Decays: Documentation of the C++ Program *AliESDv0KineCuts.cxx*". en. Bachelor's Thesis. Institut für Kernphysik, 2011.

[27] The ALICE collaboration. *ALICE Analysis Repository*. 2016. URL: https://github.com/alisw/AliPhysics (visited on 09/25/2022).

Declaration of Academic Integrity

I hereby confirm that this thesis on χ_c meson reconstruction from pp collisions at the LHC is solely my own work and that I have used no sources or aids other than the ones stated. All passages in my thesis for which other sources, including electronic media, have been used, be it direct quotes or content references, have been acknowledged as such and the sources cited.

_____

(date and signature of student)

I agree to have my thesis checked in order to rule out potential similarities with other works and to have my thesis stored in a database for this purpose.

_____

(date and signature of student)